



Collaborative Research on Novel High-Power Sources for Physics of Ionospheric Modification

**Thomas Antonsen
MARYLAND UNIV COLLEGE PARK**

**01/16/2020
Final Report**

DISTRIBUTION A: Distribution approved for public release.

**Air Force Research Laboratory
AF Office Of Scientific Research (AFOSR)/ RTB1
Arlington, Virginia 22203
Air Force Materiel Command**

DISTRIBUTION A: Distribution approved for public release

REPORT DOCUMENTATION PAGE		<i>Form Approved</i> OMB No. 0704-0188
<p>The public reporting burden for this collection of information is estimated to average 1 hour per response, including the time for reviewing instructions, searching existing data sources, gathering and maintaining the data needed, and completing and reviewing the collection of information. Send comments regarding this burden estimate or any other aspect of this collection of information, including suggestions for reducing the burden, to Department of Defense, Executive Services, Directorate (0704-0188). Respondents should be aware that notwithstanding any other provision of law, no person shall be subject to any penalty for failing to comply with a collection of information if it does not display a currently valid OMB control number.</p> <p>PLEASE DO NOT RETURN YOUR FORM TO THE ABOVE ORGANIZATION.</p>		
1. REPORT DATE (DD-MM-YYYY) 22-06-2020	2. REPORT TYPE Final Performance	3. DATES COVERED (From - To) 15 Dec 2013 to 31 Dec 2019
4. TITLE AND SUBTITLE Collaborative Research on Novel High-Power Sources for Physics of Ionospheric Modification	5a. CONTRACT NUMBER	
	5b. GRANT NUMBER FA9550-14-1-0019	
	5c. PROGRAM ELEMENT NUMBER 61102F	
6. AUTHOR(S) Thomas Antonsen	5d. PROJECT NUMBER	
	5e. TASK NUMBER	
	5f. WORK UNIT NUMBER	
7. PERFORMING ORGANIZATION NAME(S) AND ADDRESS(ES) MARYLAND UNIV COLLEGE PARK 3112 LEE BLDG COLLEGE PARK, MD 20742 - 5100 US		8. PERFORMING ORGANIZATION REPORT NUMBER
9. SPONSORING/MONITORING AGENCY NAME(S) AND ADDRESS(ES) AF Office of Scientific Research 875 N. Randolph St. Room 3112 Arlington, VA 22203		10. SPONSOR/MONITOR'S ACRONYM(S) AFRL/AFOSR RTB1
		11. SPONSOR/MONITOR'S REPORT NUMBER(S) AFRL-AFOSR-VA-TR-2020-0020
12. DISTRIBUTION/AVAILABILITY STATEMENT A DISTRIBUTION UNLIMITED: PB Public Release		
13. SUPPLEMENTARY NOTES		
<p>14. ABSTRACT</p> <p>This final report documents work conducted as part of a Multi-disciplinary University Research Initiative (MURI) in the area of active Ionospheric Modification (IM). The efforts involved four groups: the University of Maryland Space Plasma Physics (SPP) group, the University of California, Los Angeles experimental space plasma simulation group, the Texas Tech (TTech) pulsed power group, and the University of Maryland Charged Particle Beam (CPB) group. Work was divided along two interacting lines. First, UMD SPP and UCLA investigated possible mechanisms for controlling the performance of trans-ionospheric communication systems, improving the performance of submarine ELF/VLF communication systems, and possible mechanisms for controlling the flux of energetic particles trapped in the Radiation Belts (RB).</p> <p>These space plasma physics studies set the specifications for the next generation of IM heaters; addressed by the TTech and UMD CPB groups. A key difficulty concerning applications of IM is that the current research and applications rely on large permanent facilities mostly at high latitudes. The current MURI focused in the development of relatively small mobile or at least transportable facilities. The demands placed on such a transportable heater, primarily its reduced footprint in comparison with HAARP, drove the study of high efficiency sources and compact antennas. The sources investigated included laser driven Photo Conductive Solid State (PCSS) switches at TTech and high power, class D Tetrodes /Pentodes / Inductive Output Tubes (IOTs) at UMD. High efficiency sub-wavelength antennas were studied at TTech.</p>		
<p>15. SUBJECT TERMS</p> <p>EM sources, space weather</p>		

Standard Form 298 (Rev. 8/98)
Prescribed by ANSI Std. Z39.18

DISTRIBUTION A: Distribution approved for public release

16. SECURITY CLASSIFICATION OF:			17. LIMITATION OF ABSTRACT	18. NUMBER OF PAGES	19a. NAME OF RESPONSIBLE PERSON
a. REPORT	b. ABSTRACT	c. THIS PAGE			MOSES, JULIE
Unclassified	Unclassified	Unclassified	UU		19b. TELEPHONE NUMBER <i>(Include area code)</i> 703-696-9586



**Collaborative Research
On Novel High Power Sources
For Physics of Ionospheric Modification**

FINAL REPORT

<p>Distinguished University Prof. Thomas M. Antonsen, Jr., PI University of Maryland Departments of Electrical and Computer Engineering and Physics, and Institute for Research in Electronics and Applied Physics College Park, MD 20742</p> <p>Tel.: 301-405-1635 Email: antonsen@umd.edu</p>	<p>Participating Universities: University of Maryland, Departments of Physics and Astronomy K. Papadopoulos, Co-PI</p> <p>University of California, Los Angeles W. Gekelman, Co-PI</p> <p>Texas Tech University A. Neuber, J. Mankowski, Co-PIs</p>
---	--

AFOSR Grant No: FA9550-14-1-0019

AFOSR Program Managers: Dr. Jason Marshall and Dr. William P. Roach



Table of Contents

1. Overview	1
2. Objective	2
3. Approach	3
4. Main Results	4
4A. Experiments Modeling Ionospheric Modification	4
4A (a) Propagation of Alfvén waves in a magnetic beach.....	4
4A (b) Electron Bernstein waves	8
4A (c) Ferrite based antennas for launching waves in space	10
4A (d) Alfvén waves.....	11
4B. Source and Antenna Development	20
4B (a) PCSS high power switch research	20
4B (b) Optical fluence dependence of the absorption coefficient in bulk high purity semi-insulating 4H-SiC.....	22
4B (c) Fabrication and testing of a PIN 4H-SiC PCSS.....	23
4B (d) Investigation on laser wavelength impact on photocurrent efficiency	23
4B (e) Investigation of PE dependence on other parameters.....	24
4B (f) Lifetime testing and operating limit	25
4B (g) Alternate light sources for switch triggering	25
4B (h) Bond wire degradation under pulsed conditions	26
4B (i) Tunable electrically small antenna	29
4B (j) Electrically small antenna: Gap breakdown characteristics	36
4B (k) Atmospheric air breakdown by radio frequency excitation.....	40
4C. Studies of MW-Class Vacuum Gridless Electron Tubes (Tetrodes, Pentodes, and Inductive Output Tubes)	41
4C (a) Propagation of annular electron beams through the pipes with decelerating gaps.....	41
4C (b) Interaction efficiency of the device	42
4C (c) Role of secondary electrons in the device operation	43
4C (d) Extraction circuits.....	44
4C (e) Experimental studies.....	45
4C (f) Artist’s rendition of a MW-class device	47
5. Major Developments and Findings	48
6. Collaborators, Students, Papers	49

1. OVERVIEW

This final report documents work conducted as part of a Multi-disciplinary University Research Initiative (MURI) in the area of active Ionospheric Modification (IM). This work was motivated not only by its intrinsic scientific interest but also by the need to protect the critical commercial and military space-based infrastructure. The efforts involved four groups: the University of Maryland Space Plasma Physics (SPP) group, the University of California, Los Angeles experimental space plasma simulation group, the Texas Tech (TTech) pulsed power group, and the University of Maryland Charged Particle Beam (CPB) group.

The current MURI built from the success of IM research using powerful HF transmitters, known as Ionospheric Heaters that modify the properties of the ionospheric plasma by modulating the electron temperature at preselected altitudes. The most successful IM research program has been the High Frequency Active Auroral Research Program (HAARP). The HAARP heater, known as Ionospheric Research Instrument (IRI), is a phased array with capabilities far exceeding any other heater. However, HAARP is a fixed facility located at high latitude

In the present MURI work was divided along two interacting lines. First, UMD SPP and UCLA investigated possible mechanisms for controlling the performance of trans-ionospheric communication systems, improving the performance of submarine ELF/VLF communication systems, and possible mechanisms for controlling the flux of energetic particles trapped in the Radiation Belts (RB) when enhanced by a deliberate or accidental High Altitude Nuclear Detonation (HAND) or by Solar driven magnetic super-storms, such as the well-known Carrington events.

These space plasma physics studies then motivated the development of, and set the specifications for the next generation of IM heaters; addressed by the TTech and UMD CPB groups. A key difficulty concerning applications of IM is that the current research and applications rely on large permanent facilities mostly at high latitudes. The current MURI focused in the development of relatively small mobile or at least transportable facilities. Current understanding indicates that processes triggered by HF as well as VLF/ELF radio waves are strongly dependent on geomagnetic latitude. Transportable and mobile facilities will allow for the first time quantitative exploration of the IM requirements vs. geomagnetic latitude without building expensive ground installations. Furthermore proximity to application (battlefield or else) where triggering is required provides a significant advantage since nonlinear triggered processes depend on the injected amplitude and are favored by proximity. The demands placed on such a transportable heater, primarily its reduced footprint in comparison with HAARP, drove the study of high efficiency sources and compact antennas. The sources investigated included laser driven Photo Conductive Solid State (PCSS) switches at TTech and high power, class D Tetrodes /Pentodes / Inductive Output Tubes (IOTs) at UMD. High efficiency subwavelength antennas were studied at TTech.

Among the successful applications of IM uncovered by the space plasma participants were:

- **Ferrite Loop Antennae (FLA) & Magnetic Nano-Transmitters (MNT)** – Novel hybrid Rotating Magnetic Field (RMF) ELF/VLF space based transmitters that use meter length and cm diameter AC coils to drive high magnetic permeability Ferrite rods or an ensembles of Single Domain Magnetic Nanoparticles (SDMN) embedded in a non-conducting rods to

create the RMF action by flipping the rod magnetization. Laboratory tests indicate that **FLA** and **MNT** transmitters are by more than 30 dB better than conventional loop antennas while reducing their size and weight by more than 2 to 3 orders of magnitude. Applications of the new technology range RBR to creation of proton auroras at low latitudes.

- **Virtual Antennae at ELF/VLF frequencies** – These utilize the ionosphere as a nonlinear medium to convert HF (MHz) to ELF/VLF (1 Hz-10 kHz) for several DoD operations such as submarine communications and detection, underground imaging and triggering ELF-VLF emissions in the Radiation Belts for Radiation Belt Remediation (RBR).
- **Generation of Artificial Plasma Layers (APL) in the lower ionosphere** - These layers control the path of HF communication links via reflection or refraction.
- **Artificial Ionospheric Turbulence (AIT)** – Induced turbulence with control of the characteristic scale length impacts the signal to noise ratio of VHF/UHF transionospheric links including GPS.
- **Generation of trans-ionospheric ducts** – These allow injection of VLF waves to high altitudes that can trigger nonlinear emissions for radiation belt remediation (RBR).

The key findings and accomplishments of the source and antenna development work were:

- **Compact, gridless pentode device concept** - This device, driven by a 70kV, 30A electron beam, can operate in class D mode at a 0.5 MW average power level with an efficiency of about 90% at frequencies from 3 to 10 MHz. Further, it is capable of operating without any focusing magnetic fields, resulting in a compact, light-weight device.
- **Multi-stage power extraction circuit** – A tunable, multi-stage power extraction circuit, realizing high (above 90%) efficiency over the entire frequency range of interest was designed and a prototype was tested.
- **Development, characterization, and understanding of SiC PCSSs** – This includes measurement and modeling of the optical, fluence-dependent, absorption coefficient and quantification and explanation of the photocurrent efficiency.
- **Tunable, electrically small antennas** – An electrically small antenna design for a transportable heater was evaluated. With a maximum dimension of approximately 3 m, the antenna is a factor 5 – 10 times smaller than the equivalent dipole.

2. OBJECTIVE

The overall objective of the program was to identify ionospheric and magnetospheric phenomena that can be triggered by RF energy that is injected by either ground or space based sources and to develop prototypes of electromagnetic sources and antennas that can accomplish it. The program naturally divided along two lines: (i) The development of ground based transportable and reconfigurable HF sources using modern microwave technology and novel metamaterials; (ii) The development of extremely efficient, small and lightweight ELF/VLF space based transmitters that can induce triggering of Electro-Magnetic Ion Cyclotron (EMIC) emission by utilizing the energy stored in anisotropic energetic protons trapped in the inner RB.

1. **Development of ground-based mobile and transportable Ionospheric Heaters:** A key instrument in IM is the Ionospheric Heater (IH), a powerful HF transmitter that modifies the

properties of the ionospheric plasma by modulating the electron temperature at preselected altitudes. A prime example is the heater associated with HAARP. The HAARP heater is a phased array of 180 antenna units, occupying 33 acres, with 360 transmitters of maximum power 10 kW, producing radiation in the 3-10 MHz range. The facility is located at high latitude, in Gakona, Alaska. Owing to its fixed location the HAARP facility is not capable of studying IM effects that occur at mid and low latitudes where the geomagnetic field is directed primarily parallel to the earth's surface. This motivates the development of transportable heaters. The development of a transportable reconfigurable ionospheric heater is of critical importance to research and applications. In all applications proximity to the application region reduces the heater power and gain requirements and for ELF/VLF C3I systems improves S/N ratio and bandwidth. Radiation Belt Remediation (RBR) applications, Spread-F control and magnetospheric monitoring require heater location at the foot of the relevant L-shell. VHF/UHF countermeasures and bistatic communications require heater location intercepting the trans-ionospheric paths. On the research front it is well known that the response of the ionosphere to heating depends critically on geomagnetic latitude. In particular, there are major advantages for locating virtual antennas in the dip-equator. Transportable sources would allow users to conduct the needed research without building major permanent heating installations.

2. **Development of space-based ELF/VLF transmitters:** The need for developing space-based mobile transmitters was driven by recent space observations that show that constant EMIC waves with amplitude of the order of .1-1 nT trigger tone rising waves amplified by more than 20 dB. The transition from the linear to the nonlinear stage is due to a nonlinear cyclotron resonance interaction between the linearly amplified EMIC waves and energetic protons. The first one is the threshold amplitude B_{thr} for nonlinear growth that for RB conditions has typical values $B_{thr} / B_0 \in 10^{-4} \div 10^{-5}$ (B_0 is the ambient magnetic field). The second one is the saturation value) approximately 20-30 dB higher. The important point with respect to RBR objective is that the required injection energy to achieve quick remediation is the triggering energy which one thousand times smaller than the previous requirements. The showstopper in achieving this has been the extreme inefficiency of transmitters that generate EMIC waves under space conditions. A major objective of the MURI was the development of novel ELF/VLF transmitters that can increase the wave injection efficiency by 20 dB or more. Note that such transmitters will have major DoD and commercial applications.

3. **APPROACH**

Mobile and transportable Ionospheric Heater: Developing transportable heater requires interaction among team members with widely different backgrounds. In particular, space plasma physicists on the team must determine the important phenomena that can be triggered at low to mid latitudes, and define the requirements on power, frequency, and duration of the RF pulses that trigger these phenomena. This was accomplished using a combination of theory, computer modeling and laboratory experiments. The requirements were used to guide the source and antenna development. The source developers had to contend with the fact that making the heater transportable requires its size to be greatly reduced in comparison with HAARP. The consequent reduction in antenna gain implied that higher power sources must be developed to achieve the required RF intensities in the ionosphere. With the total power,

(approaching MW CW power levels) device efficiency became important. Two different technologies for sources were considered: solid state and vacuum electronic. Both had to achieve high efficiency by operation akin to a class-D mode amplifier. In the solid-state scenario, photo-conductive solid state switches (PCSSS) in push-pull configuration directly drove the antenna. In the vacuum electronic scenario, a high efficiency Tetrode /Pentode /Inductive Output Tube (IOT) drove the antenna through a tunable transformer and transmission line. The antenna system development allowed operation with either source, and a metamaterial inspired Electrically Small Antenna (ESA) approach was chosen. The ESA developed is simultaneously physically small, highly efficient, tunable, and capable of high power operation. Finally, the capabilities of the sources determined the applications that can be realized, and the impact and the direction of the theoretical and experimental ionospheric studies.

Space-based ELF/VLF transmitters: EMIC waves have frequencies below the proton gyrofrequency. They appear in three different frequency bands depending on the proximity of the different heavy ion cyclotron frequencies (O⁻, He⁺, H⁺ bands). For the inner RB of interest here the relevant frequencies range from a few 5 Hz to 300 Hz. The large capacitive reactance of electrical dipole antennae prevents their use at such low frequencies and requires non-capacitive antennas such as large loops. However loop antennas have very small radiation resistance and require large currents to achieve the required 1 nT amplitude for triggering. For example, the radiation resistance of a 20-50 meter loops at inner RB varies between $10^{-8} \div 10^{-12} \Omega$ requiring enormous currents and power to achieve the required threshold values. Alternative techniques such as Rotating Magnetic Fields (RMF) previously tested, while efficient under laboratory conditions could not be implemented in space even using superconducting coils. A joint effort by the Space Plasma Physics (SPP) group at the University of Maryland and the UCLA LAPD group examined a completely different approach to triggering EMIC waves. Instead of a large aperture loops focused on small radius (cm size) multiple loop coils with a high μ core, such as ferrite rods, tubes with ferrofluids and new materials containing superparamagnetic nanoparticles, driven by a matched AC circuit at the desired low frequency. This creates an RMF in the plasma by flipping the magnetization rather than mechanically rotating the magnet. The idea for such an antenna came from the observation that EMIC waves in magnetized plasma are confined by the magnetic field and propagate within a cone smaller than 1° providing a natural antenna gain of more than 30dB despite the small aperture. Due to cost constraints the LAPD experiments were made with ferrite rod inserts, and given the name Ferrite Loop Antenna (FLA), rather than the more optimal superparamagnetic nanoparticle inserts. A proposal for transitioning the FLA to the International Space Station (ISS) has been submitted.

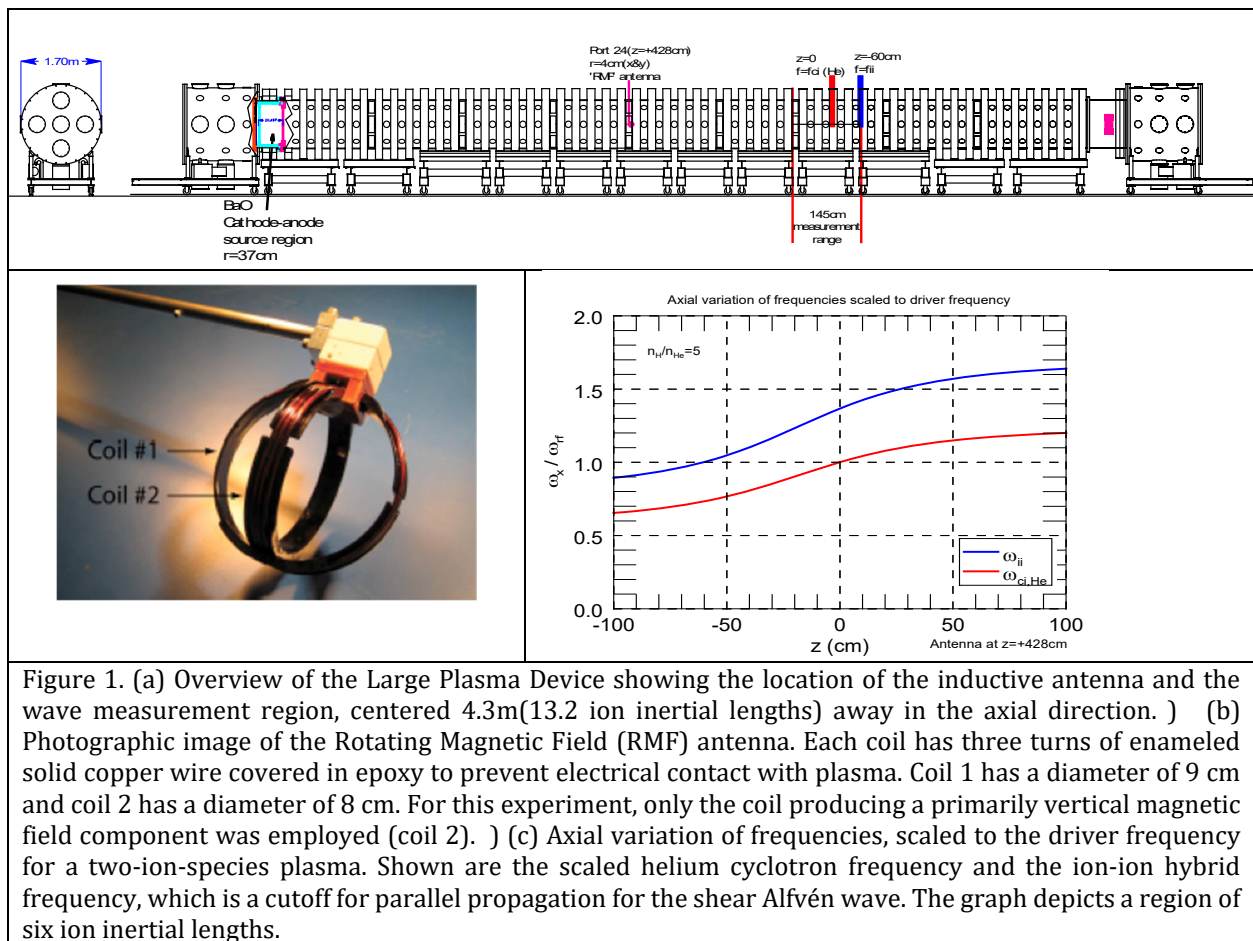
4. Main Results

4A. Experiments Modeling Ionospheric Modification

4Aa. Propagation of Alfvén waves in a magnetic beach

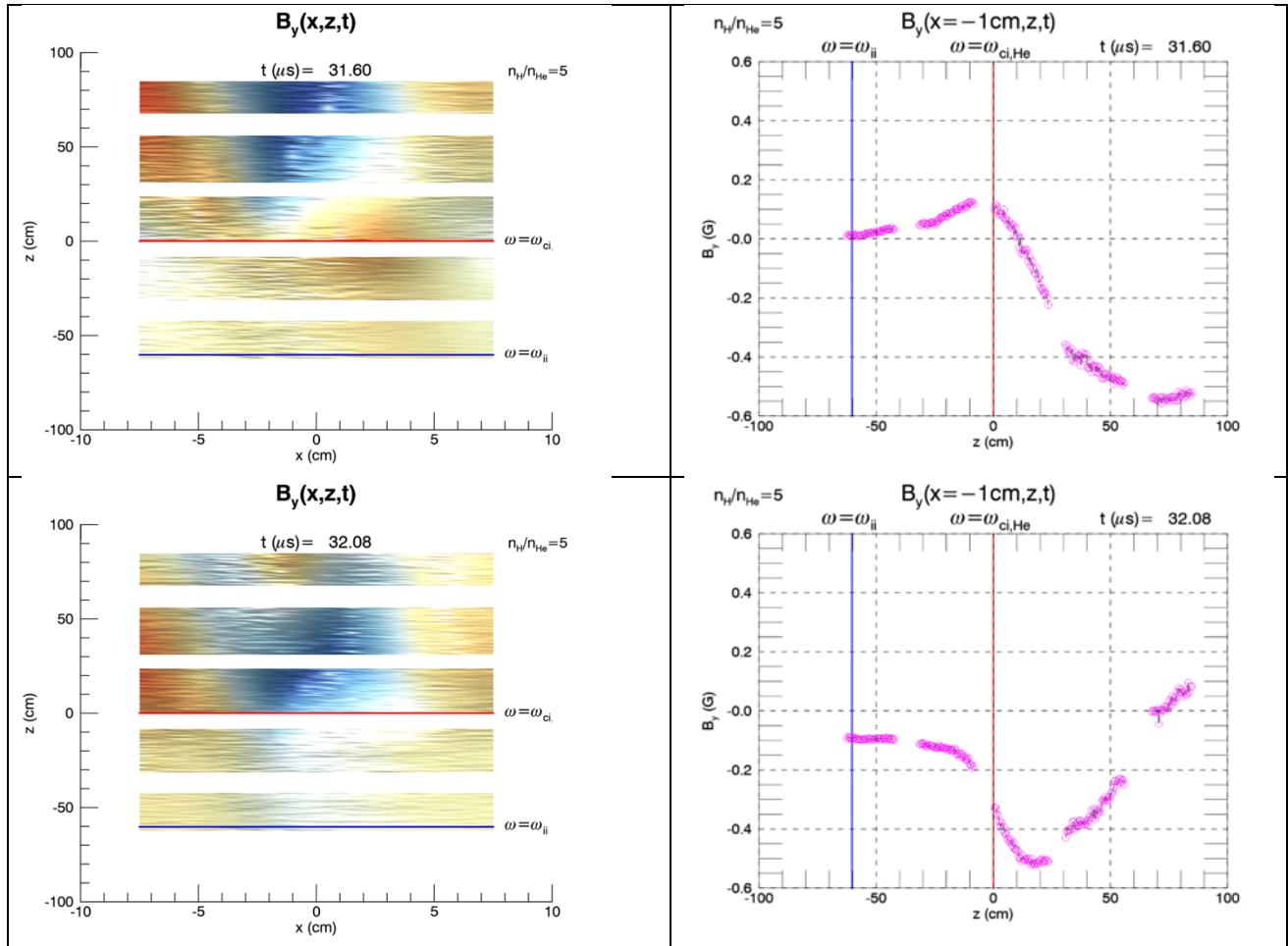
The experiments were performed in the Large Plasma Device (LAPD) [1] at UCLA's Basic Plasma Science Facility. The device contains an 18m long plasma column and can thus support

long wavelength modes. It has 450 access ports, a programmable background magnetic field and a large suite of wave and particle diagnostics. Figure 1(a) displays a schematic of the device as well as the placement of the antenna and probes. The LAPD plasma is highly reproducible and pulsed on for 10 ms at a rep-rate of 1 Hz. The LAPD plasma source is a BaO hot cathode [2]. Figure 1(b) is a photograph of the antenna [3, 4] used to launch the shear Alfvén wave. In the measurement region, a decreasing axial magnetic field results in spatially varying ratios of the wave frequency to the local helium cyclotron frequency and the ion-ion hybrid frequency. Here the plasma is composed of a hydrogen/helium mixture with the hydrogen ion density five times that of the helium density. The experiment is designed such that the wave frequency equals the helium cyclotron frequency in the center of the measurement region.



The experimental results are shown in Fig. 2. Data were acquired in five, two-dimensional planes which were in the direction both parallel and perpendicular to the background magnetic field. These measurements are necessary since the wave has finite perpendicular wavelengths and the waves propagate both parallel and perpendicular to the ambient field. In fact, the perpendicular group velocity goes to zero at the cyclotron resonance point. The right-hand column of Fig. 2 shows the y-component of the instantaneous measured wave magnetic field amplitude at three

snapshots during one-half cycle of the wave period. It should be noted that wave does not propagate beyond the cyclotron point. The left-hand column further illustrates the evanescent nature of the wave as line-outs of the 2D snapshots taken along the z-direction at the point of peak wave magnetic field. In this view, the wave is propagating from the right to the left and little wave energy reaches the ion-ion hybrid layer beyond which the wave is again expected to propagate.



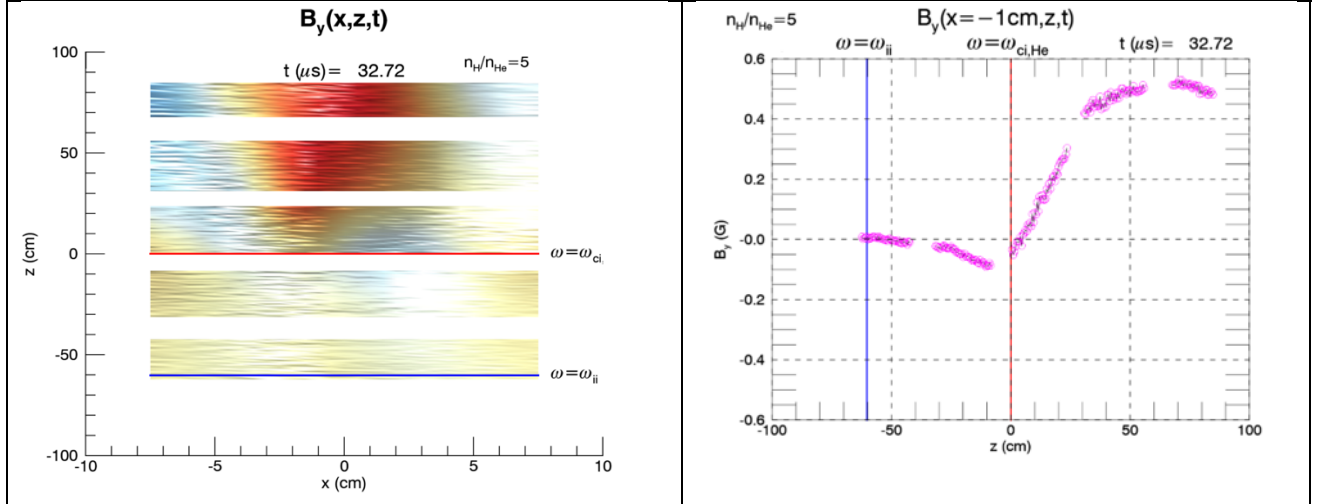


Figure 2. (Left column) Data of the instantaneous wave magnetic field amplitude as acquired in two-dimensional planes that are perpendicular (x-direction) and parallel (z-direction) to the background magnetic field. The wave propagates in the negative z-direction (top-to-bottom.) Blue indicates negative field amplitude and red indicates positive values. The three snapshots cover one half of a wave period. The wave is evanescent beyond where the wave frequency matches the local helium cyclotron frequency (red line). (Right column) Cuts of the plots in the left column along the z-axis at the peak of the wave pattern. These plots highlight the exponential damping of the wave beyond the cyclotron point, with little energy being able to reach the ion-ion hybrid layer.

In order to relate the experimental work to the theoretical predictions of Eliasson and Papadopoulos [5], we use their expression for the lifetime of a trapped relativistic electron, t_{life} , scaled to the bounce time t_B of the mirror-trapped electron:

$$\frac{t_{life}}{t_B} = \frac{\pi^2 k_{\parallel}}{8 \kappa_j} \frac{B_0^2}{|B|^2}$$

using the experimental values of $B_0 = 1000G$, $|B| = 0.2G$, $k_{\parallel} = 2\pi/100\text{cm}^{-1}$, $\kappa_{He} \approx 0.2\text{cm}^{-1}$, and bounce time given the machine length of 18m and electrons of $0.7c$ for $I_B = 1.7 \times 10^{-7}\text{s}$ to yield a lifetime of $t_{life} = 1.5\text{s}$. While this is extremely long compared with the plasma discharge of 10ms, it is important to remember that this experiment was performed in the linear regime, so that the wave amplitude was low. Other experiments have demonstrated that shear waves with $B_0/|B| = 10^2$ can be achieved with higher power drivers [3]. In this case, the predicted lifetime would drop to 600 microseconds. This demonstrates the feasibility of attempting the next stage of this experiment were we able to acquire the relativistic electron beam. Visualization of data from a two-dimensional cross-section of the plasma during the magnetic beach experiment is shown in Fig. 3.

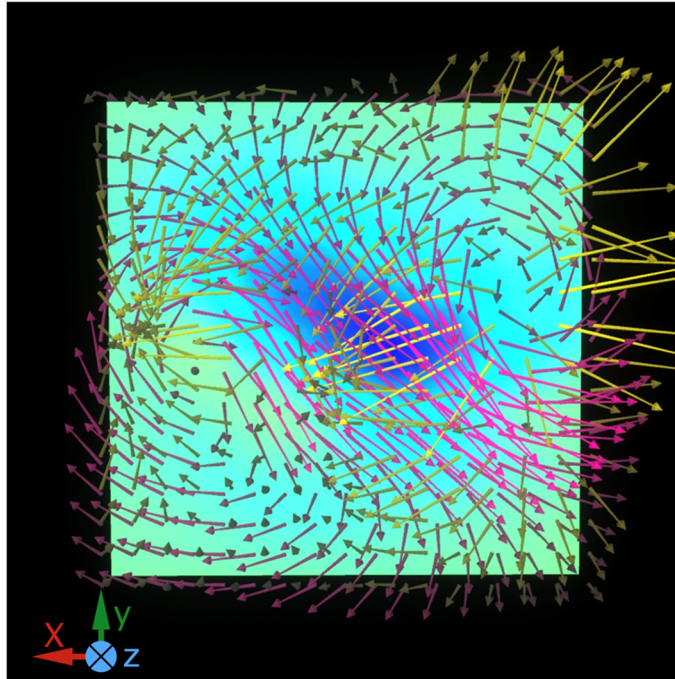


Figure 3. The image was constructed from instantaneous snapshots of both the Alfvén wave magnetic field (magenta vectors) and electric field (yellow vectors). The cross product of the two vectors is proportional to the wave Poynting flux, or wave power per unit area. The magnitude of the Poynting flux (averaged over one wave period) is shown in the solid, colored plane, which measures 20 cm on a side. Blue indicates wave power radiating away from the antenna at the center, where the wave fields are maximum and the electric and magnetic fields are nearly perpendicular. Green indicates near zero flux, and yellow indicates a small circulating power.

The ability to map the 2D structure of energy transport is a unique ability of laboratory experiments that complements the one-dimensional measurements from spacecraft and helps elucidate the global structure of the wave dynamics and energy deposition in the plasma.

4A(b). Electron Bernstein waves

In space, waves launched by ground-based heaters near the equator can produce upper-hybrid waves; if the amplitudes of these waves are sufficiently large, they can parametrically decay into electron Bernstein waves (EBWs) and lower-hybrid waves. This has been seen in simulations as mentioned in the theoretical section of this report. In the experiment, the waves were launched with a rectangular copper antenna of dimension 30 cm by 5.2 cm, with the longer side was oriented parallel to the background magnetic field. This was a linear wave experiment, where the RF amplifier which fed the antenna at frequencies up to four times the electron cyclotron frequency. The electric field of the wave was detected using a high-frequency electric dipole probe. The probe measured the spatial pattern of the wave by moving on a line perpendicular to the face of the antenna. While we have yet to acquire the tools necessary for the nonlinear parametric decay, instead this experiment was a proof-of-principle that we could detect the expected EBWs in the LAPD. Examples of the instantaneous spatial profiles of the EBW are displayed in Fig. 3. Since the phase of the RF source could not be fixed between the successive (1Hz) plasma discharges,

the amplitude and phase of the waves were obtained by performing a cross-correlation between the digitized probe signals and the antenna voltage for each discharge and for an ensemble average of 10 plasma discharges per position. Since the amplitude and phase are computed for each location, the expected backward-propagating character of the wave phase velocity was verified. The probe also detected the wave riding on an evanescent near field of the antenna. By varying the wave frequency, and measuring the resulting perpendicular wavelengths, the expected dispersion relation for EBWs

$$1 - \frac{\omega_{pe}^2}{\omega} \frac{e^{-\lambda}}{\lambda} \sum_{n=-\infty}^{\infty} \frac{n^2 I_n(\lambda)}{\omega - n\omega_{ce}} = 0 \quad (1)$$

was verified and is displayed in Fig. 4; here $\lambda = \frac{1}{2}(k_{\perp}\rho_e)^2$, and I_n is the modified Bessel function of the first kind, of order n .

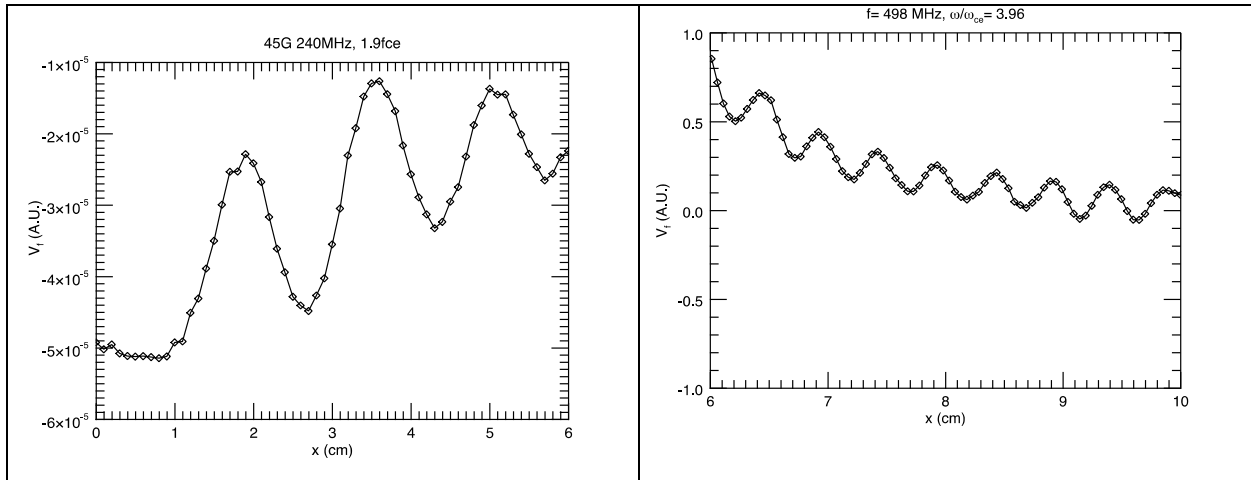
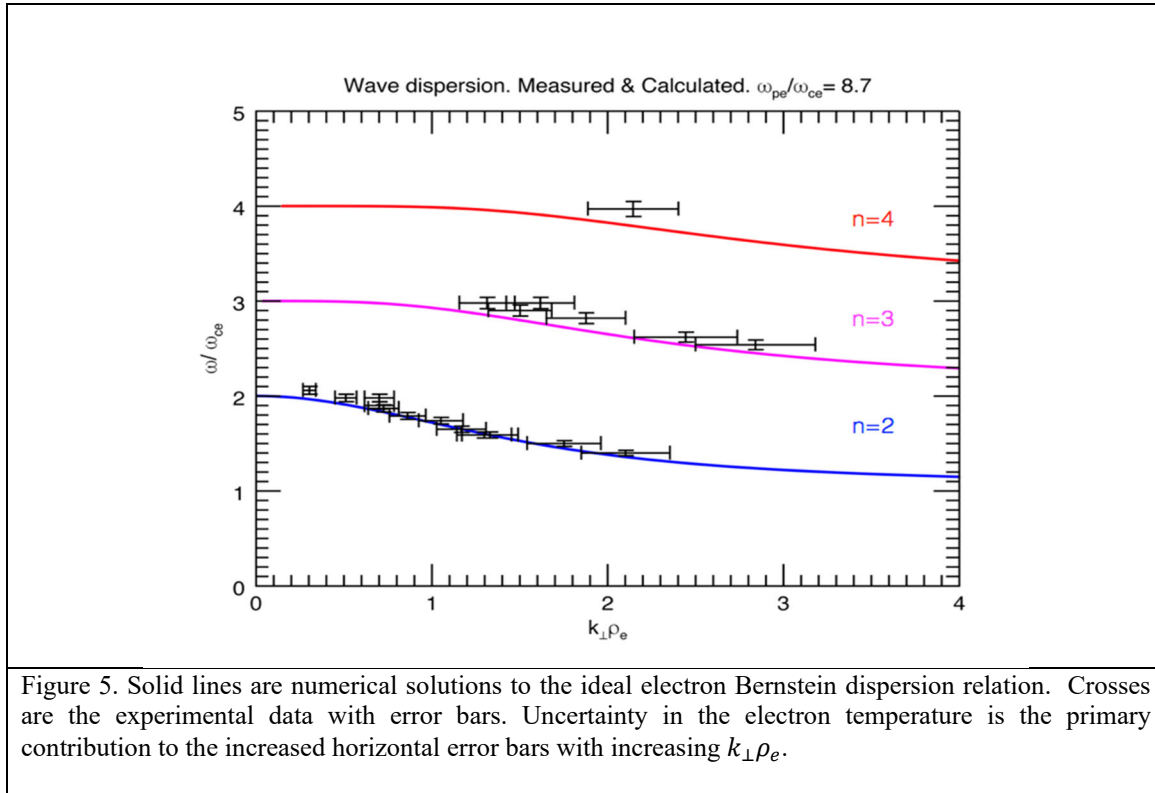


Figure 4. Select instantaneous waveforms (a) $f/f_{ce}=1.9$ and (b) $f/f_{ce}=3.96$, reconstructed from the cross-correlation between the moving probe (at floating potential) and the input waveform. Animations in time show the waves are backwards propagating — as expected for EBWs. The waveforms are a superposition of a purely evanescent wave and a sinusoidal, propagating EBW. The antenna is at $x = -1$ cm for both cases.



4A(c). Ferrite based antennas for launching waves in space

Understanding the wave-particle interactions that lead to electron and proton loss and acceleration in the Radiation Belts (RBs) is a critical issue in space physics and in the development of space weather models. In current models the description is based on interaction of relativistic electrons with quasi-static broadband whistler hiss, marginal stability and quasi-linear theory. A new understanding emerged from the high temporal and spatial resolution measurements from recent missions that emphasized short-term dynamics driven by nonlinear interactions. Until now whistler waves were thought to be the prime candidate for detrapping energetic electrons. This and previous worked funded on another MURI [6] award point to shear Alfvén, or EMIC waves as a better choice

While theoretical work was successful in reproducing many of the observed features of chorus and triggered EMIC, as well as determining the threshold amplitude required to trigger the emissions [7-12] there is lack of cause-and-effect understanding due to absence of in situ space experiments. Such an understanding is required both in order to incorporate the physics of triggered emission in space weather RB codes, and is especially true for Radiation Belt Remediation (RBR) concepts intended to precipitate trapped “MeV” satellite “killer” electrons following intentional or accidental High Altitude Nuclear Detonation [13, 14]. Given the extreme

inefficiency of conventional dipole transmitters that radiate in space plasmas [15, 16] we present a new transmitter concept. This was recently published in the Review of Scientific Instruments [17], which chose one of the figures for its cover and highlighted it on the Web.

A new transmitter concept is based on *Single Domain Magnetic Nanoparticles (SDMNs)* and is referred here as the *Magnetic Nano-Transmitter (MNT)*. *SDMNs* are small (10-20 nm radius), single domain, non-interacting magnetic grains with uniaxial magnetic anisotropy, dispersed in low viscosity, solid, or non-conducting matrices. *SDMNs* can be described as ensembles of non-interacting magnetic moments that when driven by an AC magnetic field, behave in manner similar to ordinary paramagnets. However, as *SDMNs* are composed of thousands of magnetic atoms, this means that they have susceptibilities comparable to ferromagnets but with very low coercivity and almost no hysteresis loss. The principle of operation of the MNT can be understood by considering an N turn circular loop used as antenna in magnetized plasma. The injected power P at a frequency f will be given by the $P(r,f)=I^2 N^2 R(r,f)$ where R(r,f) is the radiation resistance at a frequency f for a radius r single loop under plasma conditions. Inserting a non-conducting matrix containing the *SDMNs* into the loop will induce a magnetization $M = \mu(f)H$ where $\mu(f)$ is the magnetic permeability of the *SDMN* assembly and H the magnetic field driven by the loop current I, given by $H=I/L$, where L is the length of the ferrite. Since the equivalent current due to the magnetization M is given by $I_{eq}=ML$, the injected power will be given by $P = I^2 \mu^2 N^2 R(r, f)$. This means that the radiation resistance of the *SDMN* antenna increases by a factor of μ^2 as compared to the conventional multi-turn loop. Due to prohibitive cost of acquiring *SDMN*'s for our experiment we used conventional ferrites instead. They were enough to demonstrate the proof of principle for use of these novel antennas.

Experimental setup

The experiments were performed in the LAPD at UCLA. A schematic of the device is shown in Fig. 1. In the ferrite experiments the magnetic field was uniform and varied between $B_{0z} = 175\text{-}750\text{G}$. The wave magnetic field was measured with 3 axis magnetic probes sensitive to $-\partial B / \partial t$.

4A(d) Alfvén waves

The objective of these experiments on the generation of left-hand polarized Alfvén waves with frequencies in the vicinity of the ion cyclotron frequency (EMIC branch) was to verify the theoretical result that inserting a ferrite or *SDMN* core in an N-turn circular loop increases the radiation efficiency of a loop by a factor proportional to μ^2 and explore configurations that allow control of the injected wavelength.

We tested the radiation efficiency of the concept by using two antennas: one with a ferrite core with $\mu=30$ and the second wound on a ceramic tube of the same diameter (dia = 1 cm, length

20cm) with the normal to the loop at right angles to the background magnetic field. The ceramic wound coil had three times the number of windings as the ferrite based antenna so that the received signal would be larger and to prevent flux leakage from loosely spaced windings. Magnetic field data was acquired during the discharge and the shear wave was in the kinetic regime ($V_A \ll v_{the}$). In this test, the chamber was filled with helium plasma of density $n = 1.0 \times 10^{12} \text{ cm}^{-3}$, and with $B_z = 175 \text{ G}$, $T_e \approx 3 \text{ eV}$. The ion cyclotron frequency was $f_{ci} = 66.7 \text{ kHz}$. A ten cycle tone burst of either 50 or 85 kHz was used. Shear waves do not exist above f_{ci} as fast waves are generated instead. The antenna current was 1.6A peak-to-peak. Figure 6 shows the x-component of the magnetic field for the shear wave at $dz = 1.3$ meters at $x=y=0$ (the center of the rod).

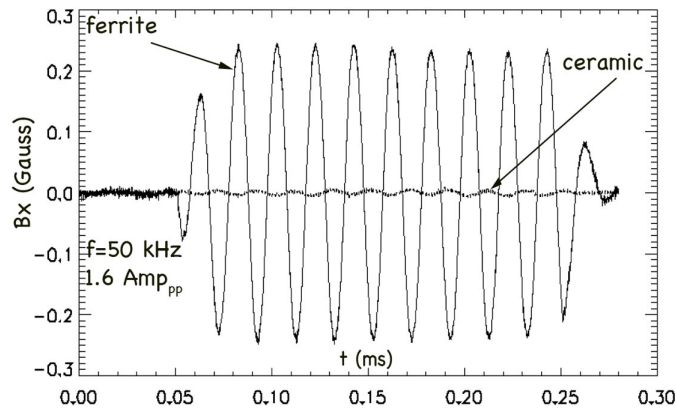


Figure 6. $B_x(t)$ at $(x,y,z) = (0,0,1.3\text{m})$, $f/f_{ci} = 0.74$. The larger trace is the wave launched using the ferrite antenna,. The amplitude ratio between the traces is of order of the μ^2 of the ferrite material (to within 25%).

The magnetic field was derived from the probe data using the area of the probe, the correction for the amplifier gain and considering the different number of turns on the two antennas. The increase in the radiation efficiency due to the ferrite insert was more than 30 dB.

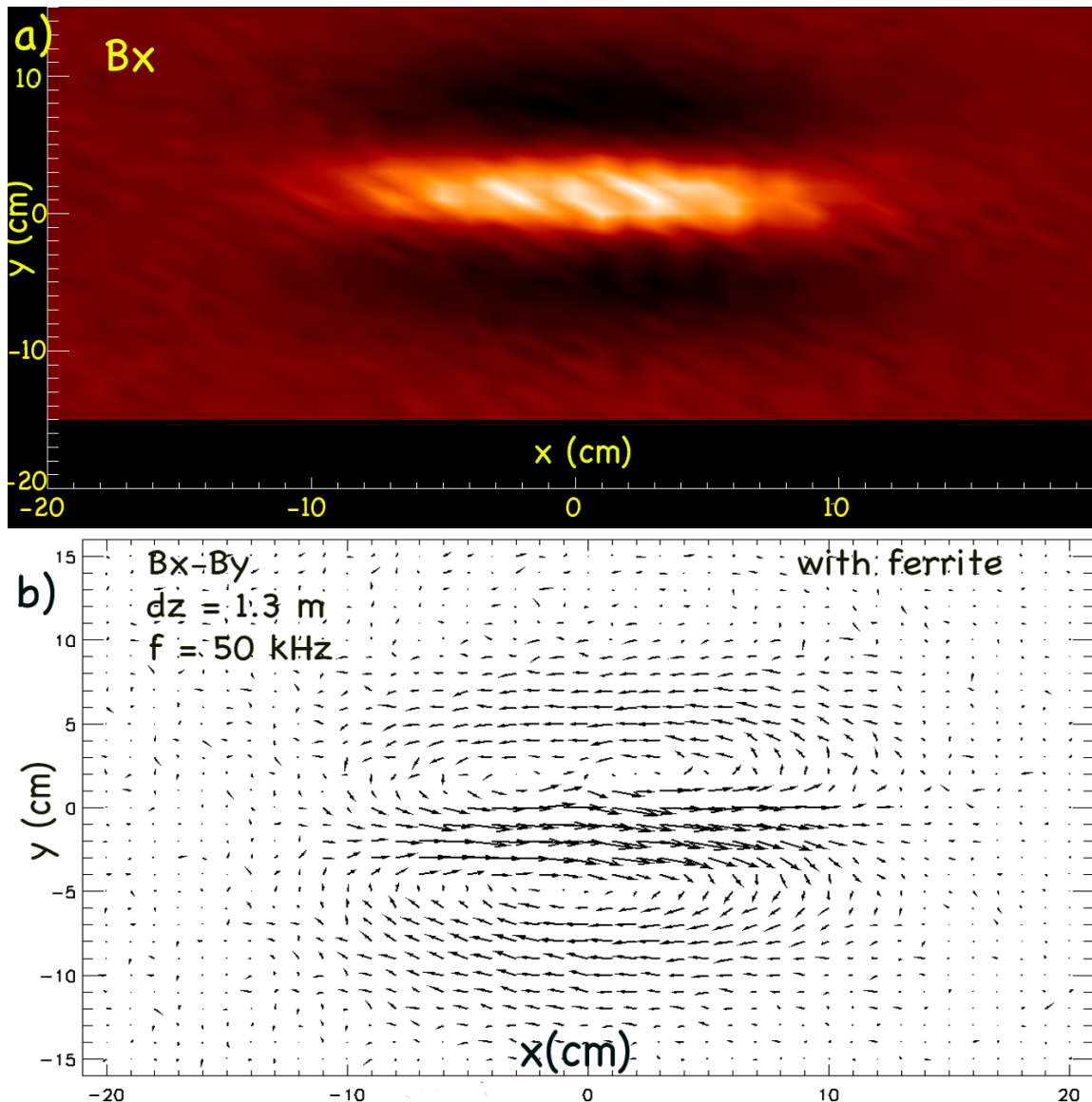


Figure 7. (a). Spatial variation of B_x at one instant of time during the RF burst for the ferrite based antenna. There is a sharp maxima (or minima depending on time) in the center flanked by two minima (maxima) above and below ($\lambda_{\perp} = 12$ cm). The parallel wavelength was not measured directly but at this density and magnetic field, $\lambda_{\parallel} = 6.48$ m. (b). Vector plot of the transverse magnetic field for the case shown in 7(a).

The measured spatial morphology of the magnitude of B_{wave} along with a vector map is shown in Figs. 7(a) and 7(b). At this time during the RF cycle, the wave amplitude is largest at the

center ($y=0$) with two minima above and below. Depending upon the number of antenna elements and their phasing, a large variety of spatial patterns is possible [18].

The wave magnetic energy density is $\frac{B^2}{2\mu_0}$ Joule/m³ and was evaluated from the data plane at $z = 1.3$ m. The largest value was 8.2×10^{-5} J/m³. The energy density of the ceramic based antenna, averaged over the entire plane, was lower by a factor of 318. In the case of a single core ($r = 0.5$ cm) illustrated in Fig. 2, the electric field was not measured directly but from using $\frac{E}{B} = V_A$ ($V_A = 2 \times 10^5$ m/s), which estimates the radiated power from the Poynting flux $\int S \cdot dA = \frac{B^2}{\mu_0} V_A A = 1.1$ W obtained by integrating the data over the device cross section. The RMS value is half of this.

Using an analysis presented in reference [17] the radiation resistance of a single loop antenna radiating in a cold magneto-plasma at an angle $\psi = \frac{\pi}{2}$ with respect to the ambient magnetic field for the conditions of the experiment He, $B = 175$ G predicted the radiation resistance of a single loop: $R_{1\text{-turn}} = 7.0 \times 10^{-7} \Omega$ without the ferrite μ and the number of loops.

$$R_{rad} = (\mu^2 N^2) R_{1\text{-turn}} . \quad (2)$$

For the wave launched by the 30 turn antenna, $\mu = 30$, $R_{rad} = 0.57 \Omega$ and the RMS power $(I^2 R_{rad}) / 2 = 0.18$ W where I is the peak current (0.8 A). This power is radiated both upstream and downstream along the magnetic field. Half of it (0.09 W) reaches the data plane 1 meter from the antenna. This is one fifth of what was measured in the experiment. This implies that the effective radius of the antenna was 0.8 cm. Since the radiation resistance goes as R_{eff}^3 this is enough to account for the difference between the predicted and measured radiation. This will be explored in a future paper.

To explore the possibility of generating small perpendicular wavelengths, which produce shear waves with considerable parallel electric fields, a 10-coil ferrite antenna was constructed as shown schematically in Fig. 8. The experiment was conducted in a helium plasma with density measured by an interferometer ($n = 2.0 \times 10^{12}$ cm⁻³, $B_{0z} = 1$ kG). Four tone bursts with $f/f_{ci} = (0.5, 1.0, 1.5, 2.0)$, core had 120 windings. Planar magnetic field data was acquired at 32 cm and 1.3 m from the exciter at intervals of $dt = 20$ ns.

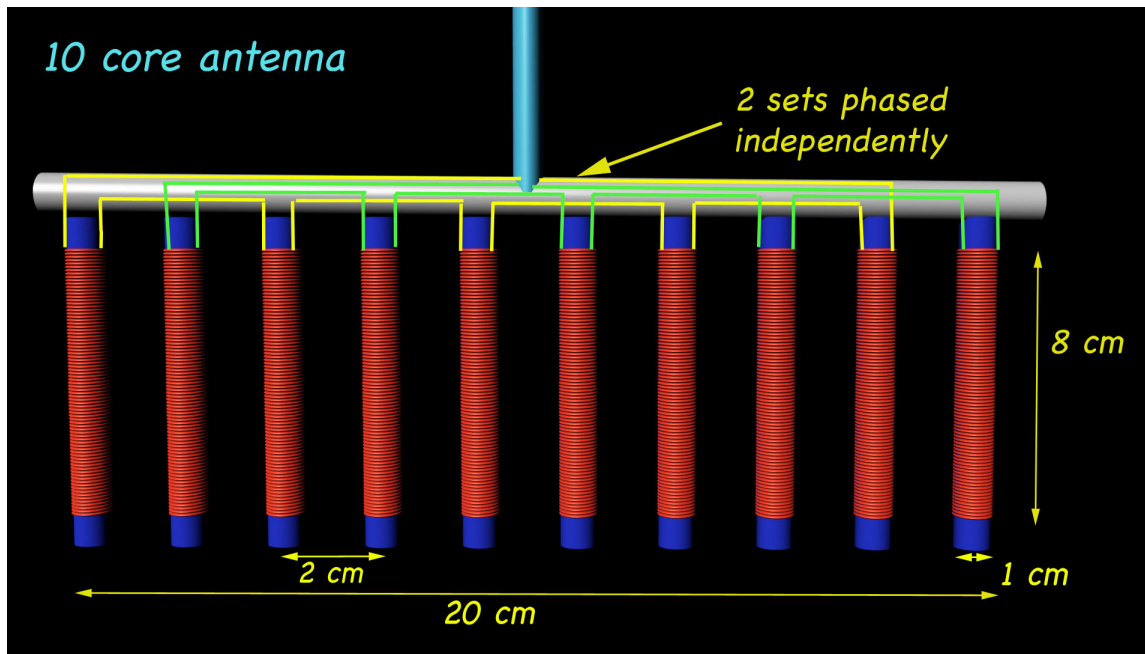


Figure 8. Schematic of 10 core ferrite based antenna. In this experiment alternate coils were driven 180° out of phase and each coil had 120 windings. The ferrite used is the same as that shown in Fig. 5. (type 78 with $\mu = 2300$ and saturation field of 4.8 kG). The background magnetic field is into the page. The plasma column is 60cm in diameter.

The largest wave component is B_y which is expected from the orientation of the antenna. From Fig. 9, the perpendicular wavelength is 5 cm. A surface plot of the magnitude of B_y in the xy plane is presented in Fig. 9. A vector plot (B_x , B_y) corresponding to the wave shown in Fig 9 is given in Fig. 10.

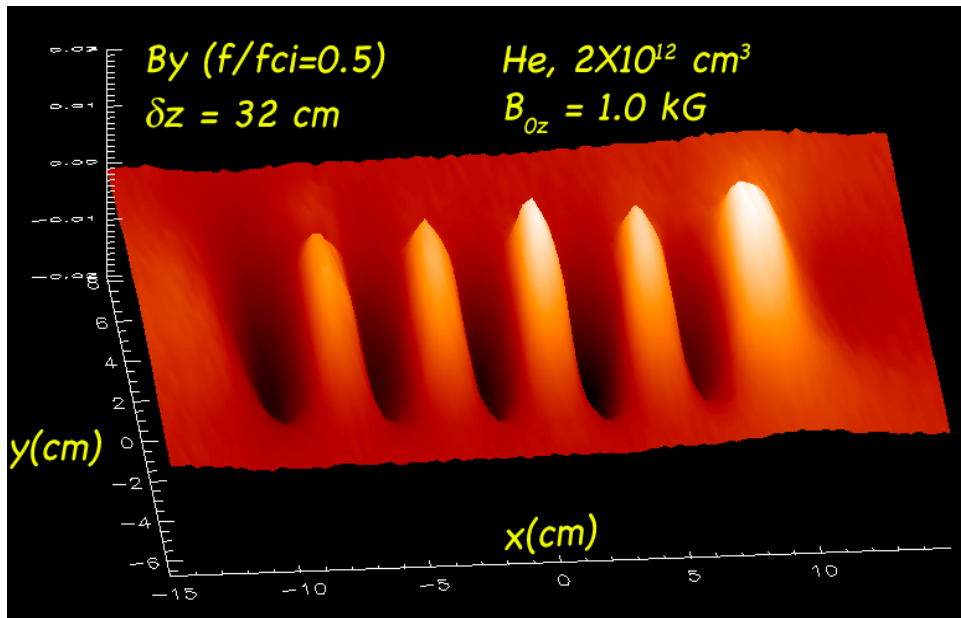


Figure 9. Surface plot of B_y for $f/f_{ci} = 0.5$. Data was acquired with step sizes of 0.25 cm in the x and y directions. The minima and maxima directly correspond to the locations of the cores. The pattern had the same spatial structure for all the frequencies explored.

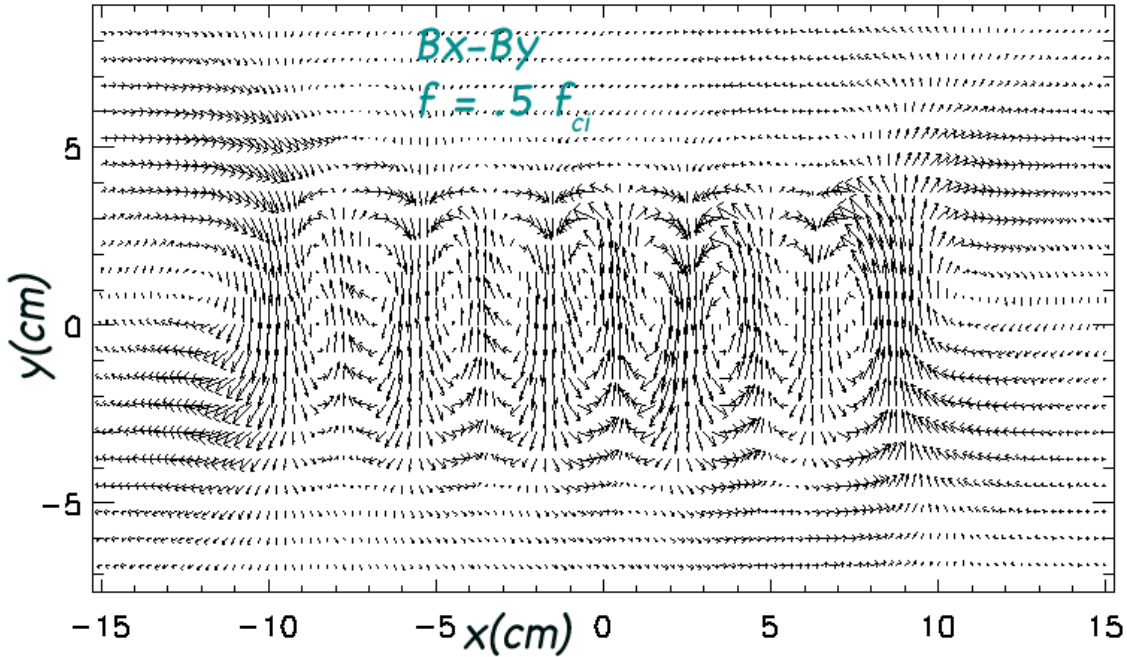


Figure 10. Vector plot of shear wave magnetic field for the 10-core antenna. The transverse wavelength can be shortened by rotating the antenna, which effectively brings the antenna elements closer together in a field-aligned projection. The result is shown in Fig.

11. A phased array of grids was previously successfully used to produce shear Alfvén waves with large k_{\perp} and the associated dispersion relation was measured [19]. This antenna was large and effectively terminated the plasma column. The antenna utilized AC currents drawn to a series of phased meshes and by its nature could only launch small amplitude waves. The ferrite antenna does not have these limitations.

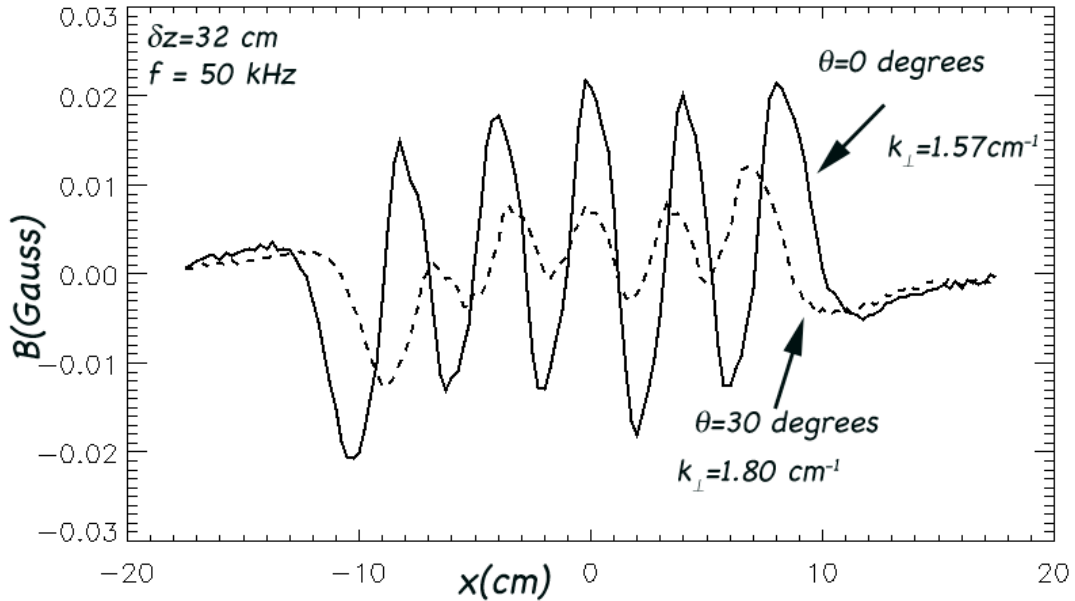


Figure 11. By component of the magnetic field as a function of x (distance across the antenna) at $y=0$. The solid line represents a zero degree rotation, while the dashed line is when the vertical support shaft was rotated by 30 degrees with respect to B_{0z} .

One measure of studying nonlinear shear waves requires a wave amplitude of order $\frac{B_w}{B_0} > 9\sqrt{\beta_e}$, where β_e is the electron beta [20]. The effective current in the antenna is multiplied by μ of the ferrite so it seems that the strong nonlinear regime can be reached by running a large current in the antenna. However before this can be achieved the ferrite may become saturated. Type 61 cores with a saturation field of 2.5kG were used in a 1kG field. A current of 0.1 A_{peak} produces a field of 1.73kG in the core, and the combination of this with the background field brings the core to saturation. Increasing the current above this had little effect. The path to large wave amplitudes lies in using ferrites that have very high saturation or using nano-particle based ferrofluids. The latter is an attractive but expensive solution.

References

- [1] W. Gekelman *et al.*, Rev. Sci. Instrum. **87** 025105 (2016).
- [2] D. Leneman, W. Gekelman, and J. Maggs, “The Plasma Source of the Large Plasma Device at UCLA,” Rev. Sci. Instrum. **77**, 015108 (2006).
- [3] A. Gigliotti, W. Gekelman, P. Pribyl, S. Vincena, A. Karavaev, X. Shao, A. Surjalal Sharma, and D. Papadopoulos, “Generation of polarized Alfvén waves by a rotating magnetic field source,” Phys. Plasmas **16**, 092106, (2009).
- [4] A. V. Karavaev, N. A. Gumerov, K. Papadopoulos, Xi Shao, A. S. Sharma, W. Gekelman, A. Gigliotti, P. Pribyl, and S. Vincena, “Generation of whistler waves by a rotating magnetic field source,” Phys. Plasmas **17**, 012102 (2010).
- [5] B. Eliasson and K. Papadopoulos, Plasma Phys. Control. Fusion **59**, 104003 (2017).
- [6] Y. Wang, W. Gekelman, P. Pribyl, K. Papadopoulos, “Enhanced loss of mirror trapped fast electrons by a shear Alfvén wave,” Phys. Plasmas **21**, 055705 (2014)
- [7] Y. Omura, Y. Katoh, and D. Summers, “Theory and simulation of the generation of whistler-mode chorus,” J. Geophys. Res. **113**, A04223, 2008.
- [8] Y. Omura and D. Nunn, “Triggering process of whistler mode chorus emissions in the magnetosphere,” J. Geophys. Res. **116**, A05205, 2011
- [9] D. Nunn, and Y. Omura, “A computational and theoretical analysis of falling frequency VLF emissions,” J. Geophys. Res. **117**, A08228, 2012.
- [10] M. Shoji and Y. Omura, “Simulation of electromagnetic ion cyclotron triggered emissions in the Earth’s inner magnetosphere,” J. Geophys. Res. **116**, A05212, 2011.
- [11] Y. Omura, and Q. Zhao, “Nonlinear pitch-angle scattering of relativistic electrons by EMIC waves in the inner magnetosphere,” J. Geophys. Res. **117**, A08227, 2012.
- [12] Y. Omura, J. Pickett, B. Grison, O. Santolik, I. Dandouras, M. Engebretson, P. M. E. Décréau, and A. Masson, “Theory and observation of electromagnetic ion cyclotron triggered emissions in the magnetosphere,” J. Geophys. Res. **115**, A07234, 2010.
- [13] Innan et al. J. Geophys. Res. **108**, 1186 (2003). doi:10.1029/2002JA0095803.
- [14] X. Shao, K. Papadopoulos, and A. S. Sharma, J. Geophys. Res. **114**, A07214, doi:10.1029/2009JA014066 (2009)
- [15] T. F. Bell, and T.N.C. Wang, “Radiation resistance of a small filamentary loop antenna in a cold multicomponent magnetoplasma,” IEEE Trans. AP-19, 517 1971.
- [16] Maria de Soria Santacruz Pich, PhD Thesis, MIT (2014)
- [17] W. Gekelman, P. Pribyl, S. Vincena, S. W. Tang, K. Papadopoulos, “Ferrite based antennae for launching Alfvén waves,” Rev. Sci. Instrum. **90**, 083505 (2019).

[18] W. Gekelman, S. Vincena, B. Van Compernelle , G. Morales, J. Maggs, P. Pribyl, T. Carter, “The Many Faces of Alfvén Waves,” *Phys. Plasmas* **18**, 055501 (2011).

[19] C. Kletzing, S. Bounds, J. Martin-Hiner, W. Gekelman, C. Mitchell, “Measurements of the shear Alfvén wave dispersion for finite perpendicular wave number,” *Phys. Rev. Lett.* **90**, 035004 (2003).

[20] T. Drozdenko, G. J. Morales, “Nonlinear effects resulting from the interaction of a large-scale Alfvén wave with a density filament,” *Phys. Plasmas* **8**, 3265 (2001).

4B. Source and Antenna Development

4B(a) PCSS high power switch research

Overview

Major contributions have been made to the development, characterization, and understanding of SiC PCSSs in three specific areas: quantification and explanation of photocurrent efficiency in bulk PCSSs, measurement and modeling of the optical fluence dependent absorption coefficient of SiC, and the design, fabrication, and testing of a PIN type PCSS. The photocurrent efficiency of bulk SiC PCSSs has been quantified over varying laser fluence ($30 \mu\text{J}/\text{cm}^2 - 30,000 \mu\text{J}/\text{cm}^2$), varying load resistance ($10 \Omega - 300 \Omega$), varying DC bias field ($8 \text{ kV}/\text{cm} - 64 \text{ kV}/\text{cm}$), and varying laser wavelength ($295 \text{ nm} - 375 \text{ nm}$). The optical fluence dependency of the absorption coefficient was investigated over fluences ranging from $1,000 \mu\text{J}/\text{cm}^2$ to $33,000 \mu\text{J}/\text{cm}^2$ and found to vary by up to 30% over the tested range.

In-house fabrication techniques were successfully developed, which culminated in the fabrication of a PIN-based SiC photoconductive semiconductor switch (PCSS). Multiple parameters were tested to characterize and understand the device concerning the photocurrent efficiency. The testing parameters included: optical wavelengths ($275 - 355 \text{ nm}$), optical fluencies ($0.5 - 900 \mu\text{J}/\text{cm}^2$), DC bias voltages ($10 - 1.5 \text{ kV}$), and load resistances ($0 - 300 \Omega$). The PIN SiC PCSS demonstrated 6 times better photocurrent efficiency relative to comparable lateral bulk PCSSs. The peak photocurrent efficiency was shown to be in the range of $305 - 340 \text{ nm}$ wavelengths. In addition, the device lifetime was proven to last longer than 10^6 switching cycles at $\sim 200 \text{ kW}$ into a 5.8Ω load. Approximately 150 PIN PCSSs were fabricated through collaboration with X-FAB Texas for the testing described.

Quantification and Explanation of Photocurrent Efficiency in Bulk SiC PCSS

Bulk SiC PCSSs have previously been found to be very good for applications requiring a high power, low jitter, closing and opening switch, capable of high ($\sim 50 \text{ MHz}$) repetition frequencies. These devices have been experimentally demonstrated to be capable of switching in excess of 4 MW into a 50Ω load at a burst repetition frequency of 65 MHz . These devices however require a large amount of optical power ($\sim 100 \text{ kW}$) to operate effectively (low photocurrent efficiency), and the root cause for this was previously unknown until this work. The effectiveness of the incident light in triggering the PCSS is described by the photocurrent efficiency which is defined explicitly below:

$$P. E. = \frac{1}{q_e} \int_0^{\infty} I(t) dt / \frac{E_{laser}}{E_{\lambda}}$$

where t is time, $I(t)$ is the current in the external circuit as a function of time, q_e is elemental charge, E_{laser} is the energy of the incident laser pulse used to trigger the PCSS, and E_{λ} is the energy per photon at the wavelength of the laser pulse. We have systematically quantified the photocurrent efficiency and found the root cause of the low photocurrent efficiency to be the

collapse of the electric field across the PCSS during the switching cycle when the PCSS resistance becomes less than the load resistance. Here we present a summary of the obtained data.

In this investigation, we found the PCSS to exhibit a maximum photocurrent efficiency of approximately 12-15% at the low energy extreme of the range tested (Fig. 12). At the highest laser fluence tested, the PCSS photocurrent efficiency was reduced to less than 1.5% and varied with load resistance. This reduction in photocurrent efficiency is due to the collapse of the electric field across the PCSS as the PCSS resistance decreases. Therefore, although bulk PCSSs have a number of advantages and are capable of high, power, low jitter switching at high repetition rates, they are inherently unable to achieve good switching performance and power delivery to the load with good photocurrent efficiency.

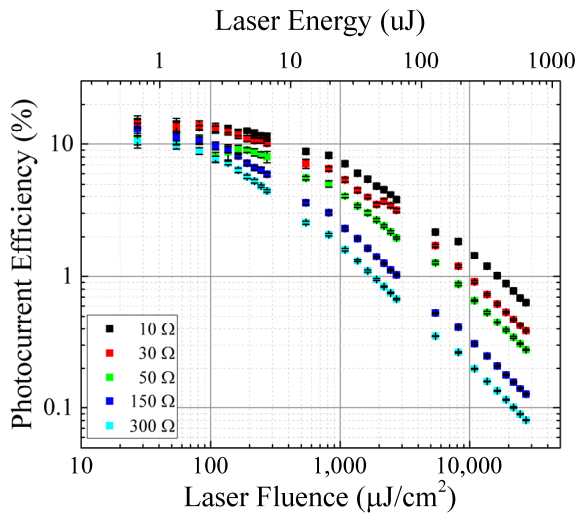


Figure 12. Photocurrent efficiency as a function of laser fluence and load resistance. As the PCSS resistance approaches and becomes less than the load resistance, the photocurrent efficiency decreases.

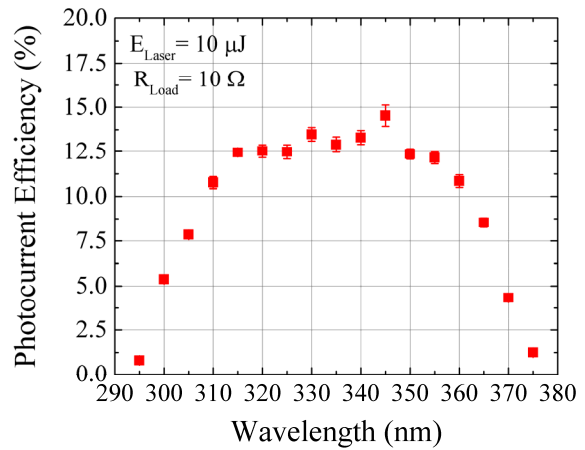


Figure 13. Photocurrent efficiency as a function of optical wavelength. The primary underlying mechanism influencing the photocurrent efficiency was found to be the changing absorption length in the material.

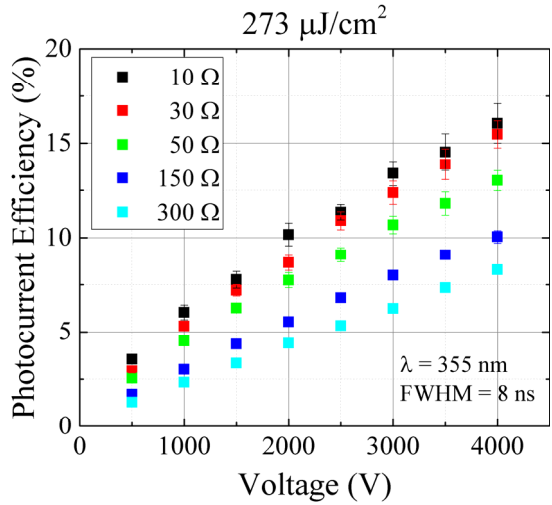


Figure 14. Photocurrent efficiency as a function of bias voltage at 273 $\mu\text{J}/\text{cm}^2$. The photocurrent efficiency was observed to be linearly dependent on bias voltage at this fluence.

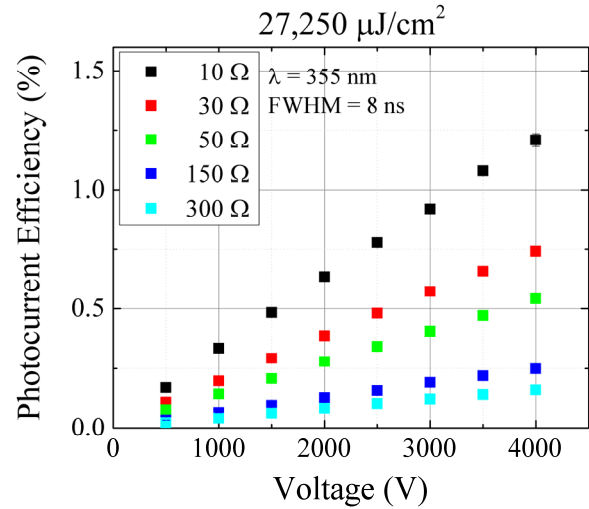


Figure 15. Photocurrent efficiency as a function of bias voltage at 27,250 $\mu\text{J}/\text{cm}^2$. The photocurrent efficiency was observed to be linearly dependent on bias voltage at this fluence.

4B (b) Optical fluence dependence of the absorption coefficient in bulk high purity semi-insulating 4H-SiC

Many investigations have been done by other research groups to quantify the absorption coefficient of 4H-SiC as a function of doping concentration, temperature, and wavelength. However, to our best knowledge, an investigation of the optical fluence dependence of 4H-SiC, specifically high purity semi-insulating (HPSI) 4H-SiC, has not been conducted. Understanding precisely the behavior of the absorption coefficient, particularly near and just above the band edge, is critical to be able to accurately model and predict the behavior of the PCSs fabricated from this material. The absorption coefficient was measured over the range of 1,000 $\mu\text{J}/\text{cm}^2$ to 30,000 $\mu\text{J}/\text{cm}^2$ at 355 nm (7-8 ns FWHM) in samples with recombination lifetimes ranging from 0.5 ns to 100 ns. The measured data is shown in Fig. 16. Modeling work was also performed to understand the underlying physics controlling the change in the absorption coefficient with varying optical fluence. This modeling work revealed that mid-bandgap defect states and free carrier absorption were the dominant physics controlling the observed behavior of the absorption coefficient. Mid-bandgap traps were found to be the dominant mechanism in samples with a low recombination lifetime, and free carrier absorption was found to be the dominant mechanism in carriers with a long recombination lifetime.

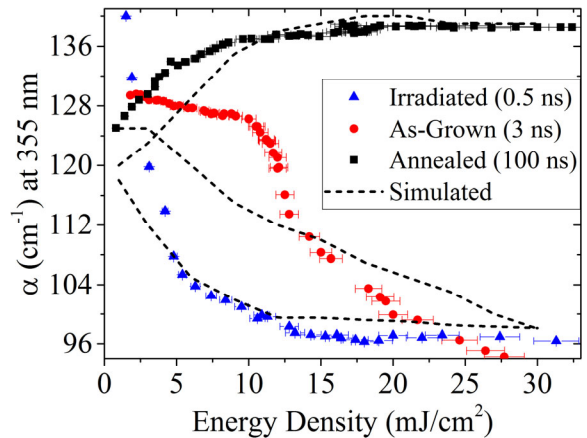


Figure 16. Measured and simulated absorption coefficient versus laser fluence at 355 nm (7-8 ns FWHM) in samples with 0.5 ns, 3.0 ns, and 100 ns recombination lifetimes.

4B (c) Fabrication and testing of a PIN 4H-SiC PCSS

In order to overcome the low photocurrent efficiency exhibited by bulk PCSSs, we have been actively developing a PIN-based PCSS. PIN PCSSs are effectively a high voltage photodiode utilized as an optically controlled switch. PIN PCSSs are fundamentally different from bulk PCSSs in that the blocking voltage is controlled by junction physics in PIN PCSSs instead of space charge limited currents as in bulk PCSSs. This therefore allows for a significantly smaller anode/cathode spacing on the order of 10-30 μm in a PIN PCSS versus 500-100 μm in a bulk PCSS. This significantly smaller anode/cathode spacing allows for a relatively high electric field to remain across the PCSS active area and still have a relatively low on-state voltage drop during conduction. This theory should allow for a PIN-based PCSS to achieve significantly ($\sim 10\times$) higher photocurrent efficiencies compared to bulk PCSSs.

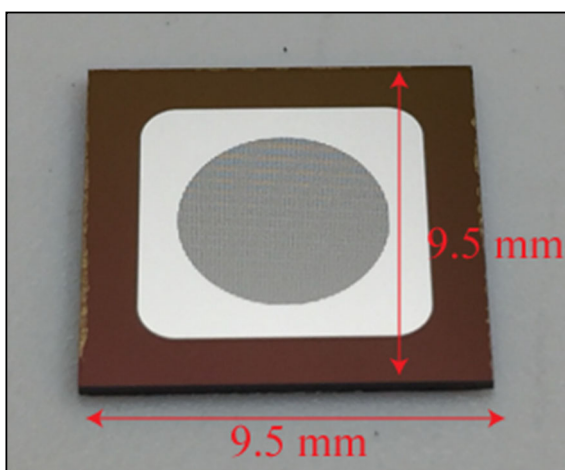


Figure 17. Diced PIN PCSS with annotated dimensions. The cathode contact is on the face shown, the anode contact is on the back-side face-down. The gridded active area (center of the die) features 10 μm metal lines with 50 μm x 50 μm open regions for coupling of the incident light.



Figure 18. Picture of the entire SiC wafer while being processed to produce the PIN PCSSs. The wafer diameter is 150 mm.

4B (d) Investigation on laser wavelength impact on photocurrent efficiency

In order to determine the optimum laser wavelength for highest photocurrent efficiency (PE), a range of laser wavelengths was investigated. Beginning at 275 nm and a DC bias voltage of 250 V, a constant laser energy of 6.5 μJ (270 $\mu\text{J}/\text{cm}^2$) was used. The wavelength sweep then increased at 5 nm increments up to 355 nm. A voltage sweep was also included in this experiment; after the wavelength sweep, the DC bias voltage was increased in 250 V increments to 1.5 kV. The results from this experiment are shown in Fig. 19. The maximum PE is shown to be in the range of 305 – 340 nm. The PE shows to have a steeper fall off from the peak in the shorter wavelength direction versus the higher wavelength direction.

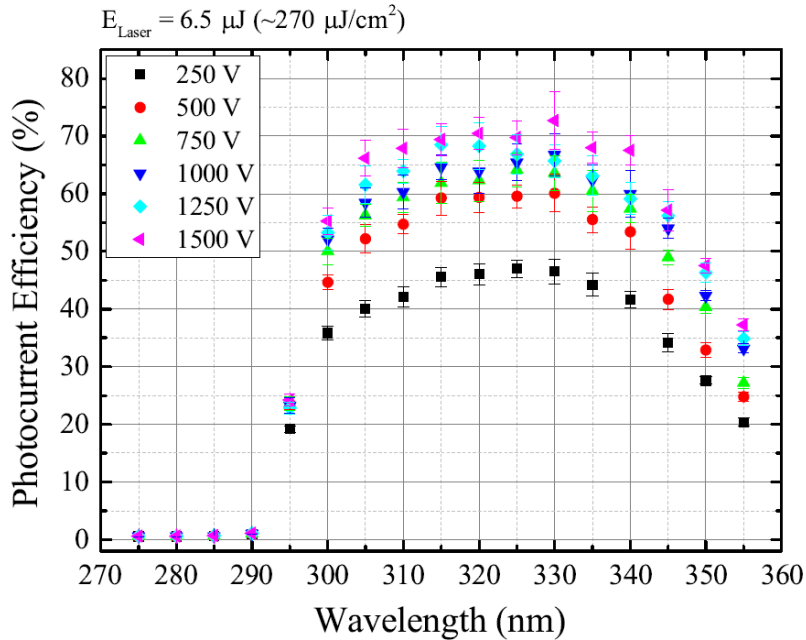


Figure 19: Photocurrent efficiency vs. optical wavelength at voltages from 250 - 1500 V. The laser energy was held constant at $6.5 \mu\text{J}$ ($270 \mu\text{J}/\text{cm}^2$). The load resistance was 10Ω , and the laser pulse width ~ 7 ns.

4B (e) Investigation of PE dependence on other parameters

Another experiment was conducted to characterize the PIN PCSS. A test matrix of varying load resistances ($0 - 300 \Omega$), laser fluences ($0.065 - 130 \mu\text{J}$ & $0.5 - 900 \mu\text{J}/\text{cm}^2$), and bias voltages ($300 - 1500$ V). In addition, the full-width at half maximum (FWHM) of the current pulse through the PCSS versus DC bias voltages with load resistance as a parameter at a constant laser energy of $130 \mu\text{J}$ was investigated, Fig. 20.

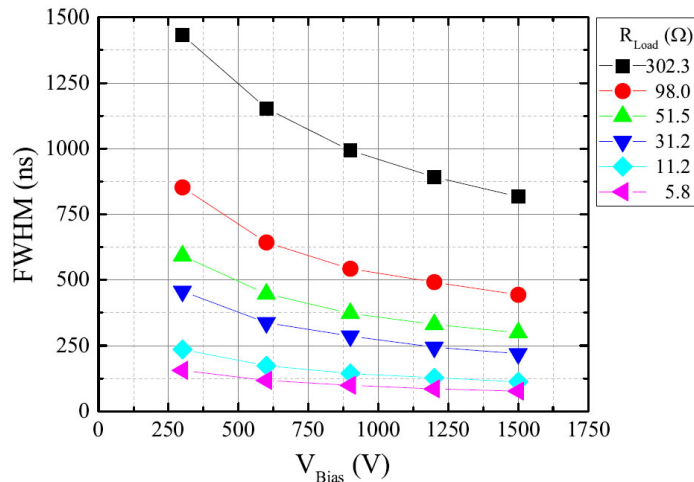


Figure 20: FWHM of the current pulse generated by the PCSS versus bias voltage with R_{Load} as a parameter. The laser energy for all data points shown was $130 \mu\text{J}$; the $R_{\text{Load}} = 0.05 \Omega$ curve is not shown due to failure of the PIN PCSS induced at current density levels $\sim 1.75 \text{ kA}/\text{cm}^2$.

4B (f) Lifetime testing and operating limit

The lifetime of the PCSS was tested with a DC bias voltage of 1.5 kV into a 5.8 Ω load with 100 μ J of 320 nm laser light. The laser switched the PCSS at a rate of 10 Hz. This resulted in the PCSS switching \sim 200 A which yields a load power delivery of \sim 230 kW. More than 10^6 successful switching cycles were performed on the PCSS with no observable degradation to the device, see Fig. 21.

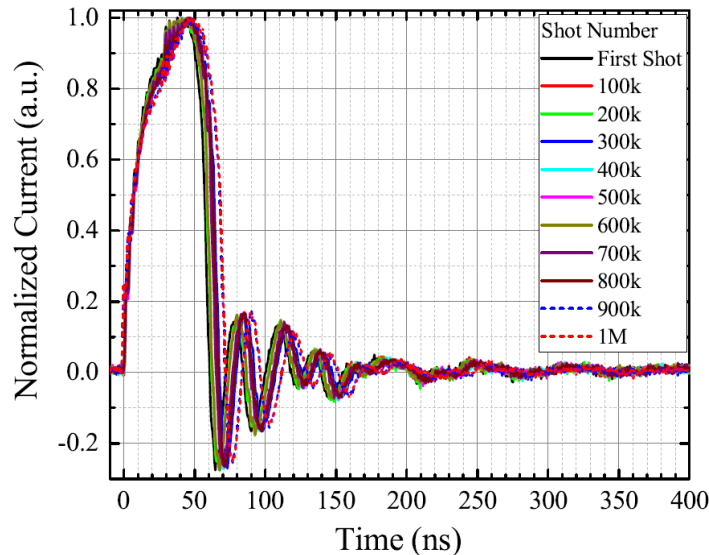


Figure 21: Current waveforms taken at selected points during the lifetime test conducted. Normalization of the current waveforms was performed to account for the shot to shot variation of the laser pulse.

Failure of the PCSSs was observed at current density levels of \sim 1.75 kA/cm². These failures occurred when the device switched into an effectively short circuit thus indicating that the failure mode is driven by excessive power dissipation at the high current densities.

Overall, three distinct trends were observed in the PE vs. optical wavelength. First, the PE increases with decreasing wavelengths from 355 nm to 340 nm. Second, the PE is effectively constant from 340 nm to 305 nm. Lastly, the PE decreases sharply with decreasing wavelengths from 305 nm to 290 nm. Further, two significant observations were made with the data obtained regarding the PE of the PIN PCSS. First, PE greater than 100% was observed which indicates a gain mechanism, such as impact ionization. Second, the PE was shown to vary with laser energy.

4B (g) Alternate Light Sources for Switch Triggering

Alternative UV light sources to trigger the PCSS based on the XeCl* (308 nm) and XeF* (351 nm) excimer sources were investigated. Three different configurations were tested: a nickel-plated micro-discharge, dielectric barrier discharge, and arc lamp. The first two sources exhibited electrical to optical conversion efficiencies \sim 1% and did not produce a sufficient amount of

optical power to effectively trigger the PCSS. The most recent UV light source tested is a pulsed arc lamp incorporating an ellipsoidal reflector, which efficiently focuses > 60% of the total light output onto the PCSS. Peak optical powers in excess of 300 W were produced with an electrical to optical conversion efficiency < 1%. With the pulsed arc lamp switching of the PCSS was possible at low current levels. The high voltage encapsulant used in the PCSS absorbs heavily in the deep UV, and therefore limits the effectiveness of these light sources. Significant improvement (> 10x) is expected by modifying the packaging of the PCSS to allow effective transmission at these wavelengths. Lastly, high power UV-LEDs were evaluated as a potential alternative PCSS trigger source. The spectral content, forward voltage, optical power, and efficiency of a commercially available UV LED in the pulsed scenario were evaluated over varying pulse width, and forward current. The evaluated LED exhibited an electrical to optical conversion efficiency in excess of 10% and produced a peak optical power in excess of 13 W. The LED was also able to trigger the PCSS into a high impedance load. High power UV-LEDs were therefore found to be promising optical trigger source for low current applications.

4B (h) Bond wire degradation under pulsed conditions

The high current densities of the PCSS switches necessitate the evaluation of wire bonding methods and wire bonding limits. Representative of wire bonding materials and sizes, the current handling capabilities of 1 mil (0.0254 mm) diameter gold cylindrical wire and 1 mil x 10 mil (0.0254 mm x 0.254 mm) Aluminum ribbon wire were investigated. The wires were bonded using TPT HB05 wire bonder unto soft bondable gold pads. The current limitations of the wires are estimated using the integral of current action. This mathematical model allows finding the time at which a bond wire will fail depending on the input current waveform. The set up consist of a test bed capable of driving pulse widths from 5 μ s to 100 μ s and sourcing current densities up to $2 \times 10^7 \text{A cm}^{-2}$. SEM imaging was used to determine good bonding conditions before the experiment as well as postmortem conditions after wire failure.

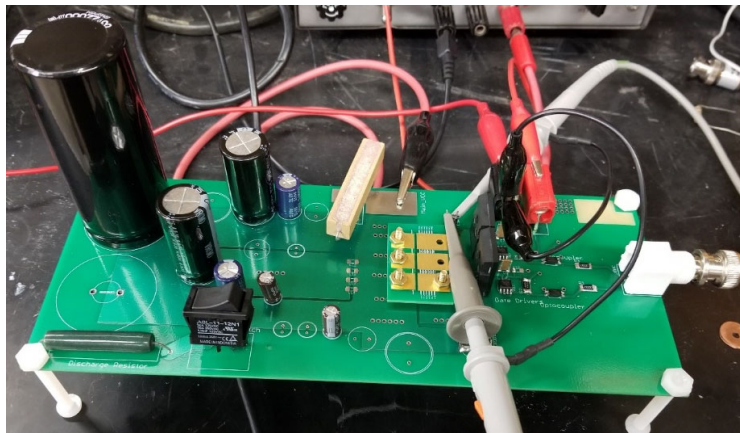


Figure 22: Test bed set up: left side capacitor bank with a safe discharge circuit, middle soft bondable gold board with test bond wires, right side CVR and MOSFETs switches with triggering signal coming from signal generator.

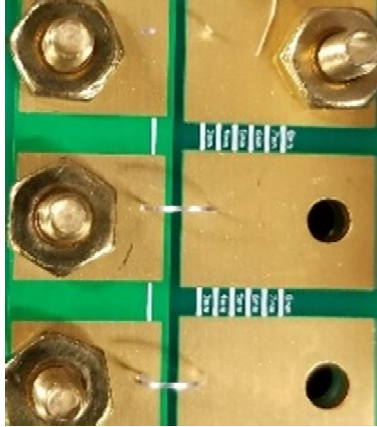


Figure 23. Anode and Cathode contacts with bond wire connecting both contacts for current to flow through the test bond wire. In this case only the top path will conduct current since the middle and right are not connected to circuit.

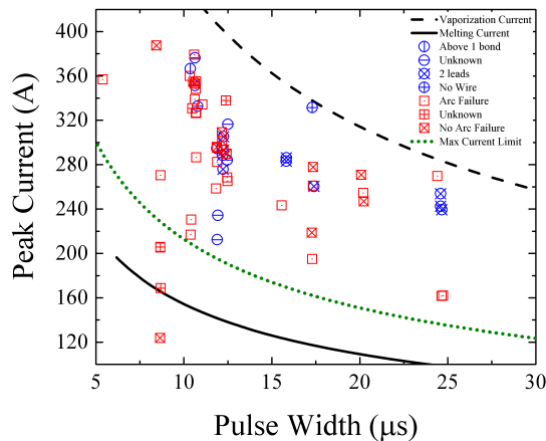


Figure 24. Graph showing different types of bond failures for the Al ribbon wire of 25.4 μm by 254 μm . A proposed maximum current limit is shown, ignoring outliers.

The test bed, shown in Fig. 22, consists of a capacitive discharge set up with the load being comprised the bond wire under test including a small current viewing resistor. The on-state resistance of the two MOSFETs switches in parallel is sufficiently low such that the current is primarily limited by the bond wire itself. The experiment procedure consists of charging the capacitor bank to a certain voltage level and then discharging it across the bond wire. If the wire survives the shot, then the capacitor bank is charged up to a higher voltage and the process is repeated until the bond wire fails. All shots leading up to the failure are saved to then be post processed. Two failure modes are being studied in this research: wire bulk failure and wire bond failure. Bond failure is diagnosed by the bond wire failing, or disconnecting, at the point of contact with the board. Bulk failure means the wire failed in a location away from the two points of contacts (Fig. 23). In one observes that a bulk failure already happened to the top most test bond wire where both points of contact are still attached to the board. The bulk of the wire can be seen disconnected from the bonds at the bottom of the cathode (top contact in the picture).

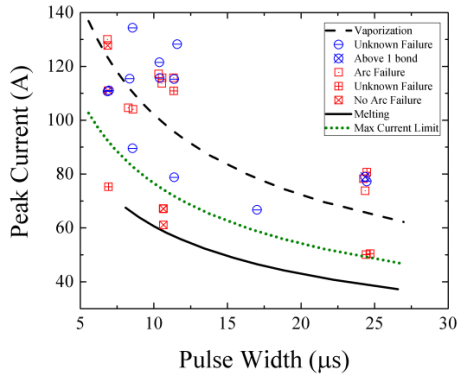


Figure 25. Au cylindrical bond wire with cross section area of $5.067 \cdot 10^{-6} \text{ cm}^2$.

The aluminum data shown in Fig. 24 shows the both the bond and bulk failures. It is worth mentioning that the bond failure includes several modes of failure varying from wire disconnection from the bond to spark explosions at the bond. In Fig. 24, *No Arc Failures* indicates no pseudo-explosion, *Arc Failure* means a pop and a current arc failure happened, *Unknown* means no failure mode was determined, and *No Failure* indicates the bond wire survived the shot. Bond failures seem to be somewhat random some happening at high peak currents while others happening at lower peak currents within the same pulse width time frame. The data points are expected to increase in peak current as the pulse width decreases. The figure also shows bulk failures for aluminum bond wires where *1 bond* indicates a failure in the bulk of the wire above the first or second bond areas, *2 leads* means that the bulk of the wire failed with only the bond sites remaining, and *No wire* means that no wire or bond sites are left on the board, lastly *No failure* indicates that the wire survived the shot. A proposed maximum current limit is shown which ignored outliers which may be used as a guideline for bond-wire specification. A proposed peak current density for Aluminum bond wires is $3.302 \cdot 10^6 \text{ A/cm}^2$ for a pulse width of $10 \mu\text{s}$ and $1.184 \cdot 10^7 \text{ A/cm}^2$ for gold. Figure 26 and Fig. 27 show the respective technique chosen for each wire. Figure 25 shows results for gold bond wires. Ball bonding being used for the cylindrical gold wire and the wedge bonding being used for the Aluminum ribbon.

A PSpice simulation was developed based on a mathematical model of exploding wires to model bond wire failures. The model uses resistivity predictions of several materials and can approximate the current response of bond wires as a function of Integral Current Action. Results from the simulation and experimental can be seen in Fig. 28. The simulation, despite being incomplete, is in agreement with the experimental measured result.

It should be noted that the experiments and simulation were carried out and assume atmospheric air surrounding the bond wires and any encapsulant will change the results. The results from doing the ICA for vaporization limit for each material having the same cross-sectional are that gold will conduct higher currents in order to reach vaporization limit, thus, gold is the preferred material for bond wires. In the tests aluminum performs better than gold due to the bigger cross-sectional area which results in a lower resistance when compared with gold. The recommendation for selecting a bond wire material and size for high current devices is to use gold

and to select the wire with the biggest cross-sectional area as possible within the parameters of the packaging size. This will result in the best performance by the bond wire.

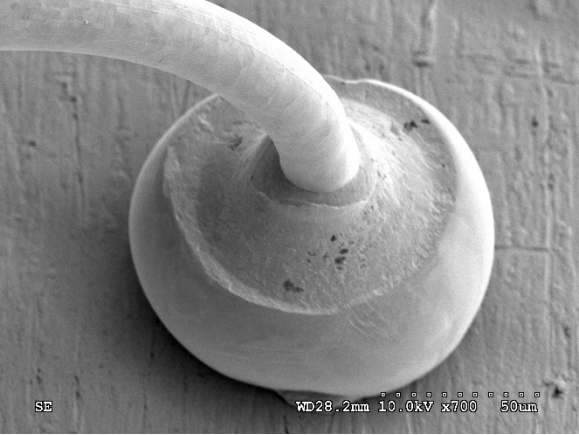


Figure 26: SEM image showing the ball bonding technique used for Au cylindrical bond wires.

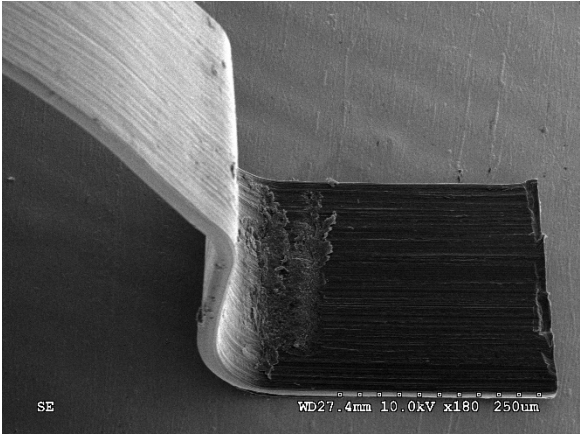


Figure 27: SEM image showing the wedge bonding technique used for Al ribbon bond wires.

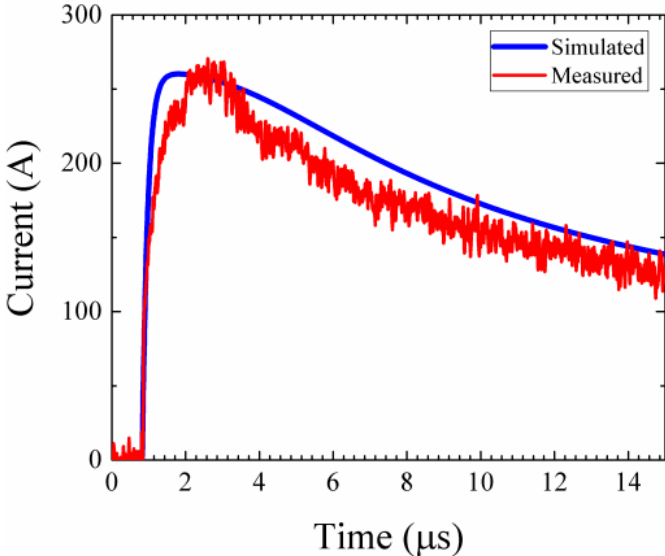


Figure 28. The result from the simulation (blue) compared to the experimental data obtained (red), follows the general shape of the pulse. Peak performance is matched; however, the inductance of each wire varies from wire to wire due to user inconsistency on loop length. Additionally, thermal radial expansion on the wire also affects the (disparity/difference) on simulation versus experimental since simulation assumes constant cross-section. On average the simulation performs well enough to be used as a good prediction of the current response of the bond wire.

4B (i) Tunable electrically small antenna

An electrically small antenna design based upon an existing design was evaluated for suitability in a transportable ionospheric heating system operating at 3–10 MHz. With a

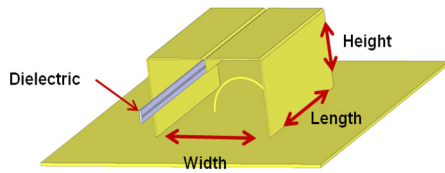


Figure 29. Isometric view of ESA with length, width, and height indicated. Included is a dielectric used for tuning.

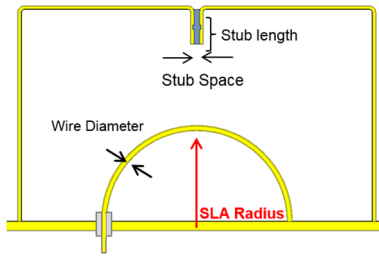


Figure 30. Side view of ESA with stub gap and length, SLA radius, and SLA wire diameter labeled.

maximum dimension of approximately 3 m, or 1/10 the wavelength of the highest frequency in air, the antenna is a factor 5– 10 times smaller than the equivalent dipole. Consisting of a Small or Semi Loop Antenna (SLA) which is coupled to a Capacitively Loaded Loop (CLL), (see Fig. 29 and Fig. 30), the antenna operates under resonant conditions with high Q and high efficiency at its design frequency. The resonant frequency of the antenna can be approximated by $f_r \cong 1/2 \cdot \pi \cdot \sqrt{L \cdot C}$ where L and C are the inductance and capacitance of the CLL, respectively. Additionally, the antenna provides a natural match to a 50 Ω source requiring no lossy matching networks which can limit power. Initially antennas were designed to be naturally resonant in small scale to ease manufacturing and testing efforts at 100 MHz with a fixed coupling between SLA and CLL and tuned to lower frequencies using insertable dielectrics in the capacitive gap of the CLL. Using lossy dielectrics or ferrites results in large power losses in those lossy materials and with

sufficiently high power for long CW excitation will melt the dielectric or heat a ferrite above the Curie temperature which ends with a loss of material properties. Regardless, using the common dielectric PTFE (Teflon®) a tuning range of 83–100 MHz was observed as the dielectric is inserted. Eccostock HiK®, a ceramic based microwave dielectric ($\epsilon_r = 15$, $\tan(\delta) = 2 \cdot 10^{-3}$) produced a tuning range of 32 – 100 MHz. Radiation efficiency is reduced due to additional losses introduced by the dielectric, dropping to 21% at the low frequency end of the tuning range where radiation efficiency is defined as the ratio of transmitted (radiated) and accepted (not reflected by port) power. Reflection losses additionally lower total efficiency with reflection coefficients of worse than -6 dB at the lower frequency end. Following verification of the ESA scalability, a full-size ESA designed for operation at 10 MHz was simulated, optimized, fabricated and tested. With a 9.7 x 7.2 m ground plane, this antenna experimentally demonstrated a gain of 5.8 dBi, and a HPBW of 114.4°. Calculations estimate the power capability of this antenna design to be in excess of 1 MW with an air dielectric. Simulations predict a gain of 7.3 dBi and a HPBW of 62.3° with this antenna mounted on a barge in seawater. The full-scale model was also used to test the feasibility of a direct drive method, for instance with a PCSS, where the antenna is driven via a square pulse train. Radiated power reached approximately 500 W for a 200 V DC charge input with approximately 90% efficiency. The antenna effectively filtered out harmonics and radiated a sine wave with minimal harmonics (> 40 dBc).



Figure 31. Full-scale prototype ESA used to test gain, pattern, and direct drive feasibility.

A collaboration with UNM resulted in a design which utilized a horizontal gap and no lossy materials for tuning, see Fig. 32. A tuning range of 44 – 99 MHz was simulated with overlap ranging from 3 to 23 cm and a gap spacing of 0.5 cm. Results for a full-scale antenna are similar, albeit at a factor 10 smaller frequency range. The full scale 5 cm gap has the benefit of increasing CLL breakdown strength thereby allowing for higher power. Efficiency stays high across the range at 88.3 to 99.4% at the low and high frequency end, respectively. Losses in this case are mainly attributed to conductor losses which scale with frequency and skin depth. At lower tuned frequencies, the Q of the CLL increases along with current creating a larger conductive loss. With high efficiency across its tuning range, Fig. 33, the horizontal gap is a promising design for an ionospheric heater array. However, the inherent asymmetry in the design introduces a variable shift in radiation pattern, which is dependent on both the frequency and ground plane size, Fig. 35.

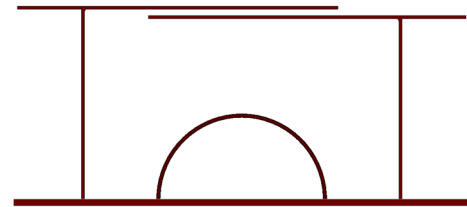


Figure 32. Side extrusion view of the horizontal gap antenna. Two overlapping plates are used to adjust the capacitance and thus tune the antenna.

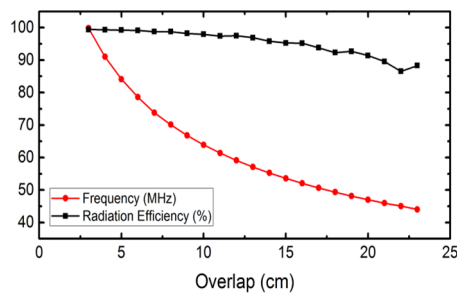


Figure 33: Efficiency and Resonant frequency vs horizontal plate overlap.

A physical lumped element circuit model revealed the ability to improve coupling at the low frequency end of tuning range simply by reducing the coupling between SLA and CLL. Three methods to achieve this reduction in coupling were simulated in CST MWS to determine viability. As a first order approach, to prove the theory, the SLA was simply rotated along its z-axis.

Reflection of greater than -25 dB was achieved at 70° (Fig. 36). This method, while functional, is not easily implemented and as such two additional methods were explored. The SLA may be held stationary at the grounded end with the feed point pivoted around this point, resulting in better than -20 dB reflection. And most promising, a method comprising of leaning the SLA along its x axis, Fig. 35, was finally explored. All three methods resulted in the reduction of coupling between SLA and CLL and improved matching dramatically, summarized in Fig. 36. Furthermore, this method was confirmed to function at 32 MHz on the previous 100 MHz prototype antenna improving reflection from -7 to -30 dB.

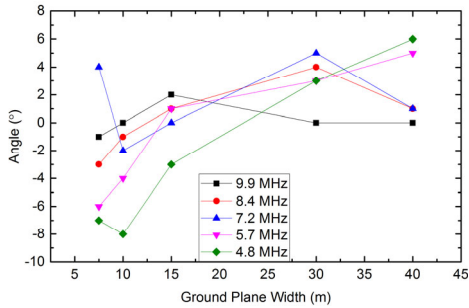


Figure 34. Angle of maximum gain vs ground plane size for various tuned frequencies.

A theoretical array consisting of 24 ESA elements arranged upon two ocean going barges, visualized in Fig. 37, achieves 23.8 dBi of gain with a half power beam width of approximately 11°.

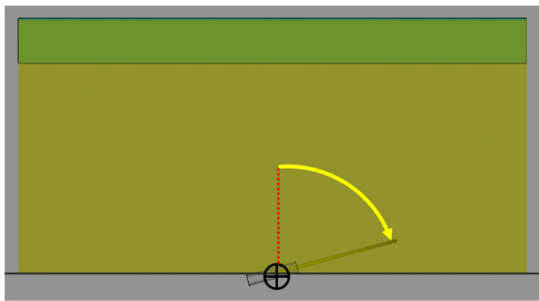


Figure 35. Side view of ESA showing direction of SLA lean and axis of rotation.

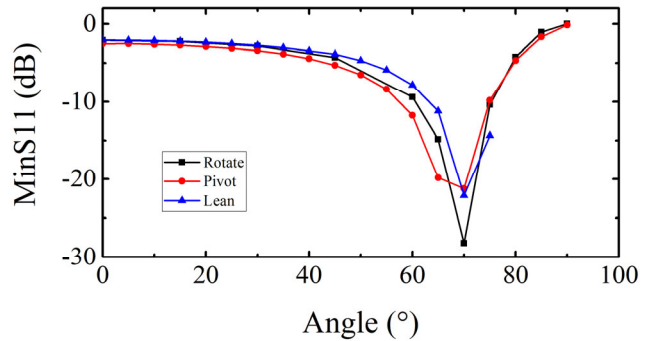


Figure 36. Minimum S11 (reflection) vs angle of SLA. Best matching occurs at approximately 70°.

With spacing of 0.75λ the effects of mutual impedance should be minimized however electrical spacing will decrease with frequency making those effects more evident. Such an array

has the capability of affecting 2,690 km² of the ionosphere, approximately 4.8 times larger and area than HAARP with a total transmitted power of 24.6 MW, or 683 kW per antenna element. As a first order estimate, primary power efficiencies of approximately 80% is achievable owing to the lack of matching networks and potential direct drive capability. To generate an ERP equivalent to HAARP, an array input of 24.6 MW is required, or 30.8 MW primary power. To summarize, the barge array footprint is 10 times smaller than HAARP, requires approximately 3.2 times higher primary power and affects an area 4.8 times larger. Power requirements and beam width can be improved with additional elements; however, this complicates such a transportable array. This mobile array allows for ionospheric research at any location accessible by water.

A small 4x4 array of ESA's could be used for virtual antenna ELF generation studies with an ERP of 80 dBW. A power level of 1.496 MW (93.5 kW per element) would be required with a gain of 20.4 dBi.

A hinged antenna design, with simulated tuning range 30 – 105 MHz in small scale and shown in Fig. 38, has been explored including the assembly of a 1/10th scale prototype shown in Fig. 39. Stepper motors and a pulley system are used to tune both the capacitive gap and SLA angle for coupling tuning with a custom controller based upon a readily available 3d-printer control board. The coupling tuning method reduces the coupling between SLA and CLL at low frequencies and improves reflection coefficient by an order of magnitude. As this design uses no dielectric for tuning, it is desirable in that losses will be low, thus retaining high efficiency across its tuning range with 5 dBi of gain in simulation – falling off to 2.35 dBi at the 45 MHz. However, a large plate area is required, 21 m² at the low end, making the antenna tall. This may be mitigated if the antenna were to be made longer, for example 4.6 m, which would make the height requirement of the gap reduced to 4.6 m as well. Unfortunately, due the large size required for the capacitive gap, this design is no longer electrically small, by definition at its higher frequencies, as the radiating body now occupies a space larger than the Wheeler radian sphere. A benefit of this design compared to the horizontal plate design is the symmetrical radiation pattern. The angled plates do induce a field gradient with the highest field at the bottom where the plates are closest. Careful field enhancement mitigation will be required to avoid breakdown in this area. A 10 cm gap was shown through simulation and physical experiments to be capable of handling 500 kW CW with a gap area of 21 m².

The constructed prototype achieved a tuning range of 33.56 – 117.5 MHz with a point of best matching at 105 MHz. Coupling tuning, via angling of the SLA, was implemented improving the port match, Fig. 40. The SLA used was likely slightly large and the results seen here may be improved with a smaller SLA. S11 improved from -2 dB without coupling tuning applied to -15

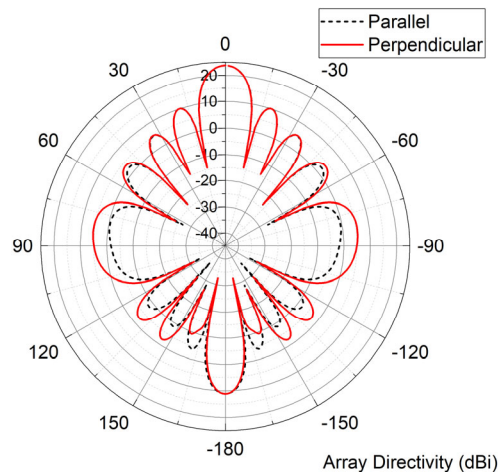


Figure 37. Two-barge array pattern with 20.9 dBi of gain in addition to antenna gain is observed.

and -8 dB for the 48 and 33 MHz cases, respectively. Q factors of 109.7 to 18 at 50.1 and 104 MHz were measured, or 1.4 to 1.7 times the Chu limit.

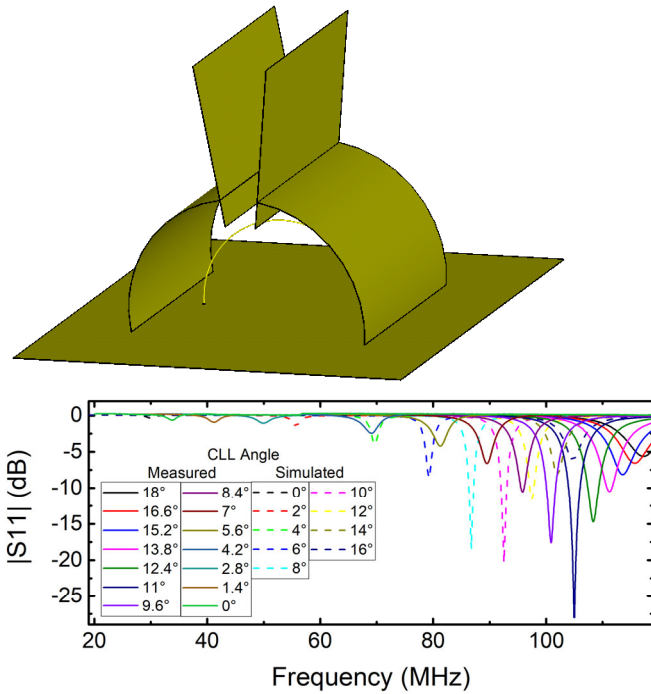


Figure 38. Top - EM model of hinged vertical gap antenna with SLA visible. Bottom – Simulated and measured reflection coefficient of vertical gap antenna with CLL included angle varied. High reflection at low end is improved via reduction of coupling between SLA and CLL.

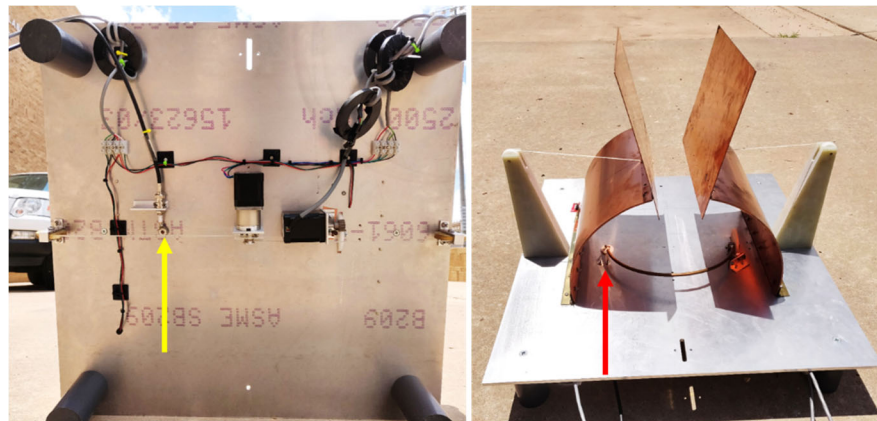


Figure 39. View of constructed prototype petal antenna with capacitively loaded loop fully open and small loop antenna (SLA) at minimum coupling (left). Stepper motors control both capacitively loaded loop and SLA through a pulley and gear system, respectively (right). Also shown is SLA feed point fed via 50 Ohm coaxial line, indicated by arrows. Control lines loaded with ferrites to reduce common mode noise and EMI.

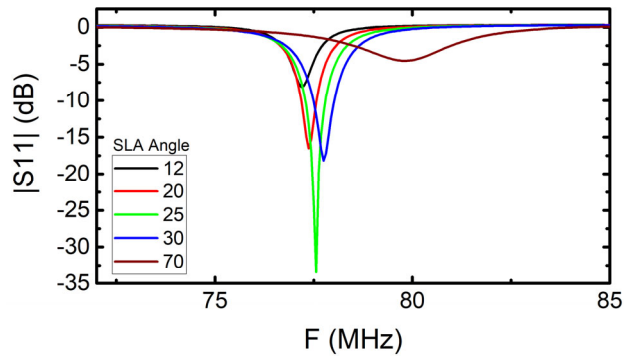


Figure 40. Experimental coupling tuning at approximately 77 MHz. Best $|S_{11}|$ with SLA at 25° , capacitively loaded loop at 5.6° .

Array cross talk, or mutual inductance, between elements in an array was studied to give an understanding of radiation and port effects. A 2×2 array of the basic ESA design, Fig. 41, with 0.75λ spacing at 10 MHz was simulated in CST 2014 with all structures meshed and solved and

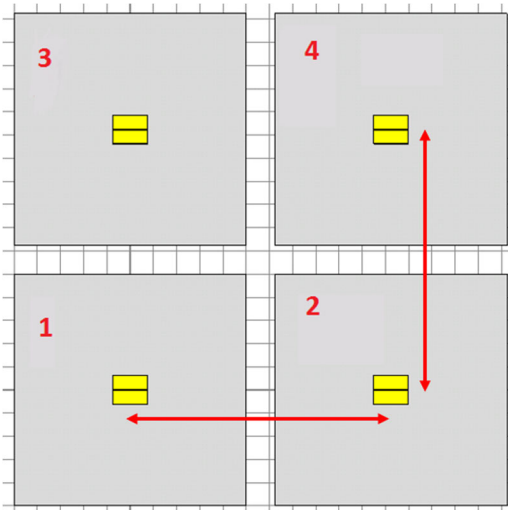


Figure 41. 2×2 array shown with 0.75λ (10 MHz, ~ 22.5 m) spacing shown with arrows. Coupling is highest between elements 2 and 4 where capacitive gaps are parallel.

in-phase excitation. Maximum gain available was slightly reduced at all frequencies with largest effects at the lowest frequencies due to decreased electrical separation. In general, the magnitude of mutual coupling follows A/r^2 where r is the center to center distance between elements, and A is a coefficient determined by antenna shape, array layout, and other constant factors. At 10 MHz coupling is low, -19.8 dB for parallel capacitive gaps, where coupling between elements is highest amongst orientations tested. At 4 MHz, coupling increased to -10 dB with electrical spacing reduced to approximately $1/3 \lambda$, again for parallel gaps. Antenna port impedance is not significantly affected given that launched and reflected waves are similar between antennas, being only slightly shifted to lower frequencies. An in-phase antenna array may be effectively driven with little modification needed. Beam angle steering will likely affect these

characteristics and should be considered.

Lastly, a further understanding of the differences and correlations between an equivalent circuit, Fig. 42, and physical EM structure was developed. From a lumped circuit perspective, the coupling coefficient between SLA and CLL must increase with decreasing frequency to match EM simulations without consideration for coupling tuning. Since the physical structure does not change, this change in coupling coefficient may be explained by a frequency dependent change in apparent inductance of the SLA and CLL due to parasitic capacitances in the physical structure. This change in apparent inductance may be assumed to follow the equation $L \cong L_0 \cdot (1 + \omega^2 L_0 C_p)$ where L_0 is the DC inductance of the CLL and C_p is the parasitic

capacitance. Thus, in a circuit simulation where inductances are kept constant, the coupling coefficient appears to decrease with frequency. The parasitic capacitance of the CLL was found to be approximately 13 pF. Coupling tuning may be implemented in the circuit model as a simple reduction of coupling coefficient which includes the change in apparent inductances of both the SLA and CLL, ranging from 0.126 to 0.03 (~ 19% of original value) at the high and low end respectively.

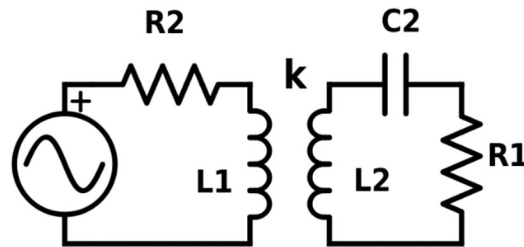


Figure 42. Equivalent circuit model for ESA. R2 and L1 represent the SLA, with L2, C2 and R1 representing the CLL. k is the coupling coefficient between the two. The parasitic capacitances which exist in parallel with L1 and L2 are not shown.

4B (j) Electrically small antenna: Gap breakdown characteristics

Due to the design and planned operating power of the electrically small antenna, a study was conducted in order to characterize the high voltage breakdown threshold between the capacitive gap. An experimental setup was designed and implemented in order to recreate antenna gap conditions, see Fig. 43. In order to ensure the effectiveness of the experimental setup, DC breakdown measurements were taken and compared with literature. Steel and brass electrodes incorporating spherical (1.9 cm diameter) and a Bruce profile (10 cm diameter) were used. The Bruce profile was used in order to provide a uniform electric field as to avoid field enhancements towards the edges and ensure breakdown in the main body of the electrode. Results followed in principle with a breakdown equation for air (in kV) from Lao

$$V_s = 24.4pd + 6.53\sqrt{pd}$$

where p is gas pressure in Torr and d is the electrode gap distance in cm. This equation is used to compare the measured DC breakdown results. Although the equation does not take certain factors into account such as humidity, it is still an acceptable comparison. Figure 44a shows the average DC breakdown measurements compared to the equation above. Six shots were taken at each gap spacing, while waiting one minute between shots. After six shots, the electrode surfaces were cleaned a Kimwipe soaked in an acetone solution to remove surface contamination accumulated from breakdown. The experimental setup may be driven in RF mode with breakdown results in Fig. 44b utilizing the RF driver depicted in Fig. 45. Measured breakdown field data using Bruce profile electrodes followed well with the breakdown equation curve. The breakdown field data using brass spherical electrodes began to deviate from the breakdown equation curve at smaller gap distances. This is believed to be a consequence of the smaller size and shape of the electrode as the electrode area is known to play a crucial role in the overall feedback mechanism. It is less

probable for a photon emitted from the excited gas molecules to find the cathode for photoemission of an electron if the cathode is physically small.

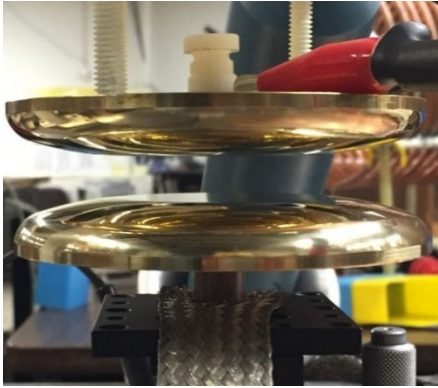


Figure 43: Gap spacing setup using electrodes incorporating the Bruce profile.

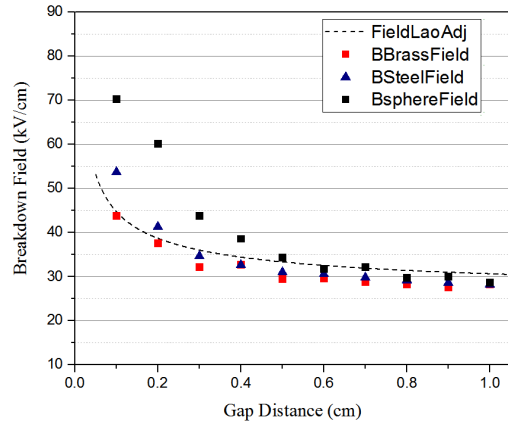


Figure 44a: DC breakdown field results from a 0.1 cm gap to a 1 cm gap using stainless steel and brass electrodes Bruce profile electrodes and brass spherical electrodes. DC measurements compared to breakdown equation (Lao).

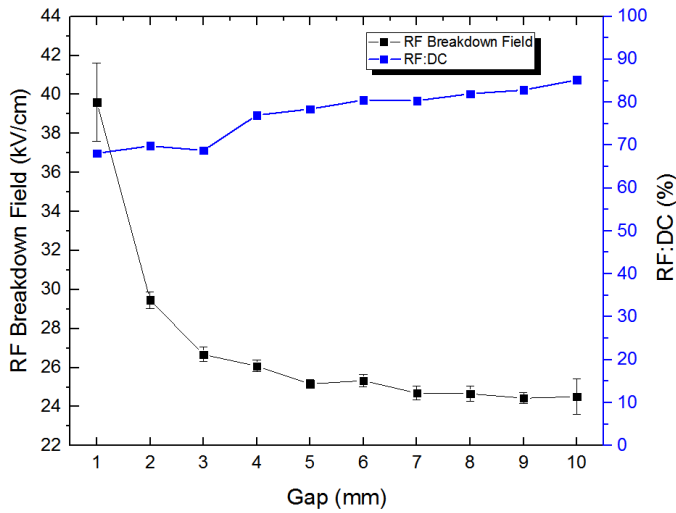


Figure 44b. RF breakdown field at 0.1 – 1 cm gap distances in ambient air for RF breakdown setup tuned to 3.3 MHz with 10 cm diameter polished Bruce profile stainless steel electrodes.

To generate the required RF voltages, a series of RF amplifiers is connected to L1 (small loop) of the setup shown in Fig. 45. This energy couples to L2 (large loop), with the coupling tuned for highest Q of the system. L2 in series with the combination of the electrode gap and vacuum capacitor form a resonant LC tank which drives the voltage to kV levels. The RF amplitude is measured through a capacitive voltage divider.

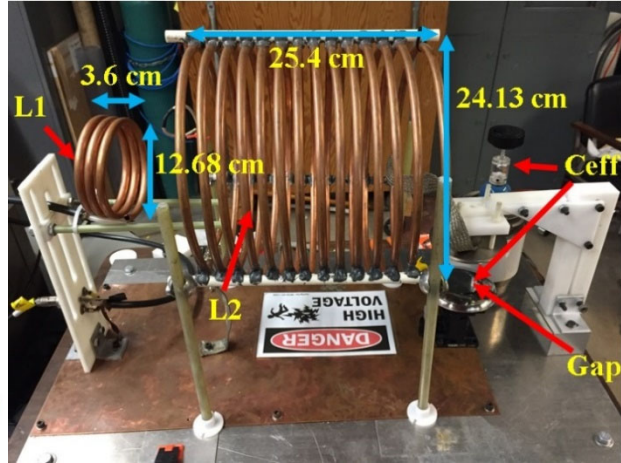
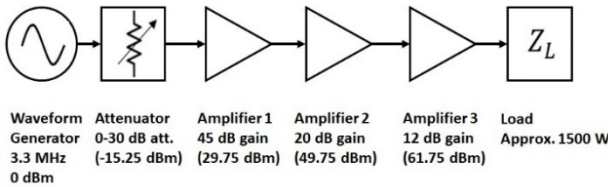


Figure 45. Schematic representation of the RF signal source path (left) and photo of the RF experimental setup (right). Coil L1 couples power from RF amplifier into the LC tank. Vacuum capacitor for tuning LC tank operating frequency. Electrode gap with interchangeable electrodes (Stainless steel Bruce profile electrodes shown).

Results indicate that RF breakdown is approximately 80% of DC values, matching trends as simulated (see section “Atmospheric Air Breakdown by Radio Frequency Excitation”). RF breakdown with voltage rise as fast as ~ 1400 V/ μ s were measured and analyzed using stainless steel Bruce profile electrodes. Measurements were taken with and without the illumination of UV in the electrode gap seeding electrons. This was done to compare with experimental results with the results corroborated by another student’s Monte Carlo simulation focused on the inclusion of photon processes which assume many electrons in the gap. RF breakdown field measurements under UV illumination followed reasonably close with simulation results, c.f. Fig. 46.

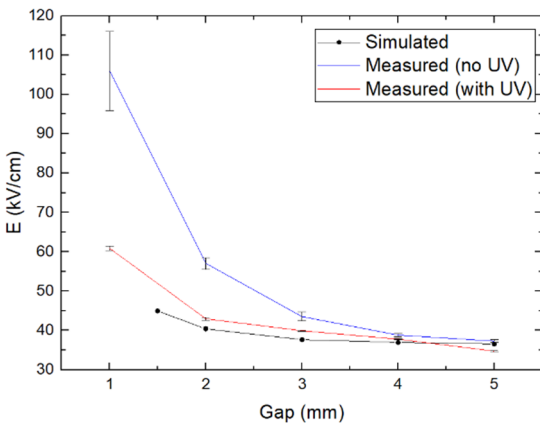


Figure 46. Fast rise time RF breakdown (with and without application of UV) compared with Monte Carlo simulation results. Measured data for 1-5 mm in 1 mm increments. Simulation results are given for 1.5-5 mm.

Because corona losses are always a concern in high power RF transmission systems, RF corona at 3.3 MHz in atmospheric conditions were also recorded. The electrode configuration used a stainless-steel Bruce profile electrode paired with a tungsten needle for a 2 cm gap in a needle-plane geometry. The RF corona utilized the same source for the RF breakdown experiments. The tungsten needle features a 47.6 mm tapered length, 250 μ m tip, and 6.36 mm base width. Based on measured data graphed in Fig. 47, the onset power needed to ignite RF corona in a 2 cm gap in the LC circuit is approximately ~ 23 W rms.

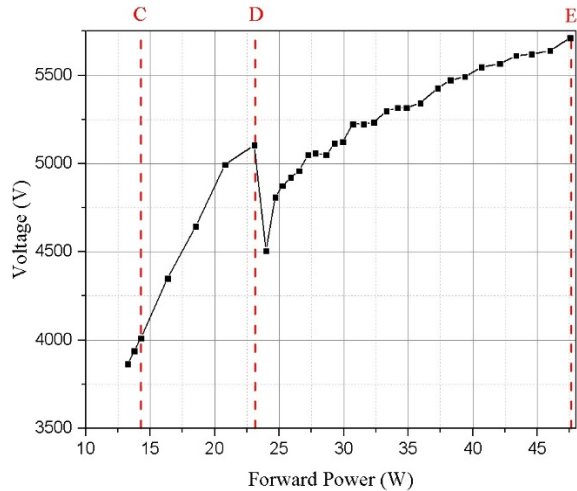


Figure 47. RF corona voltage measurements with respect to applied rms power at 3.3 MHz. Power is incremented by 0.1 dBm steps after reference line D. Reference line D: RF corona onset power; Reference line E: RF breakdown power; Reference line C: RF corona extinguish power.

Based on the presented measurement data, an estimated limit for the ESA with a 10 cm minimum gap at 3.3 MHz would be approximately 845 kW with a gap voltage of ~260 kV. At 500 kW, the ESA electric field of ~20 kV/cm may be safe for operation. RF corona measurements demonstrated the need to eliminate any sharp protrusions in the ESA capacitive gap to avoid corona losses.

4B (k) Atmospheric air breakdown by radio frequency excitation

The breakdown dependence in air at atmospheric pressure subject to RF excitation was studied through numerical modeling. Frequency changes over orders of magnitude (from DC to 100 MHz) were analyzed. Most previous studies of RF breakdown had focused on the field dependence on pressure. Also, unlike previous reports, our focus was on much larger gap lengths in the 0.5-5 cm range. A numerical analysis, with transport coefficients obtained from Monte Carlo calculations, was used to ascertain the electric field thresholds at which the growth and extinction of the electron population over time are balanced. The Monte Carlo code was validated by comparing the predicted results with measured data. For example, the field dependence of the electron impact ionization coefficient (α) as obtained from the Monte Carlo simulations is shown in Fig. 48. The numerical results compared well with numerous experimental data points.

Results for the atmospheric breakdown by radio frequency excitation are shown in Fig. 49. Our simulations resulted in a U-shaped frequency dependent breakdown field characteristic. The results indicated lower breakdown fields with increasing gap lengths, and trends qualitatively similar to the frequency-dependent field behavior for microgaps. Simulation results obtained for the breakdown field strength versus operating frequency for two different (1 and 3 cm) gap lengths are shown in Fig. 49. The low frequency value of ~34 kV/cm for a 1 centimeter gap is seen to approach the reported DC Paschen limit. More faithful reproduction of measured results requires the inclusion of photon effects in the simulation including photoionization of gas and photoemission at the electrodes. Comparing simulation results which include photon effects to measured values obtained with large area electrodes from 1 to 5 mm indicates the validity of the simulation, shown in Fig. 50. The results can also serve as a useful guide to determine the safe operating voltage limits at various frequencies in atmospheric air. The voltage ranges at the higher frequencies, however, may be practically difficult to attain based on current technology.

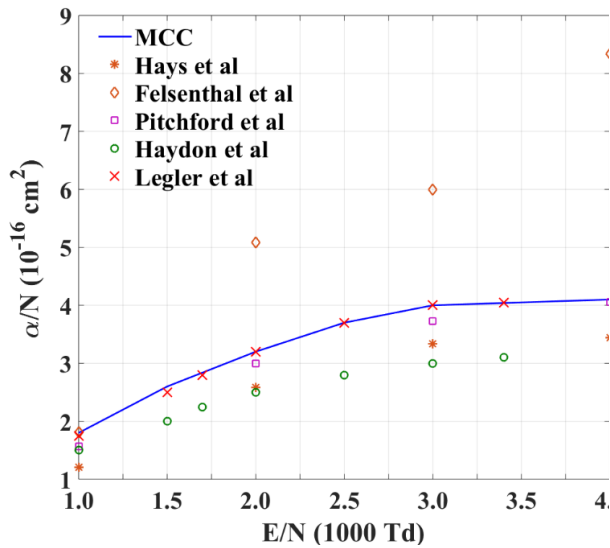


Figure 48. Predicted field dependence of the electron impact ionization coefficient (α) as obtained from Monte Carlo simulations. Numerous experimental data points are shown for comparison, and good agreement is evident.

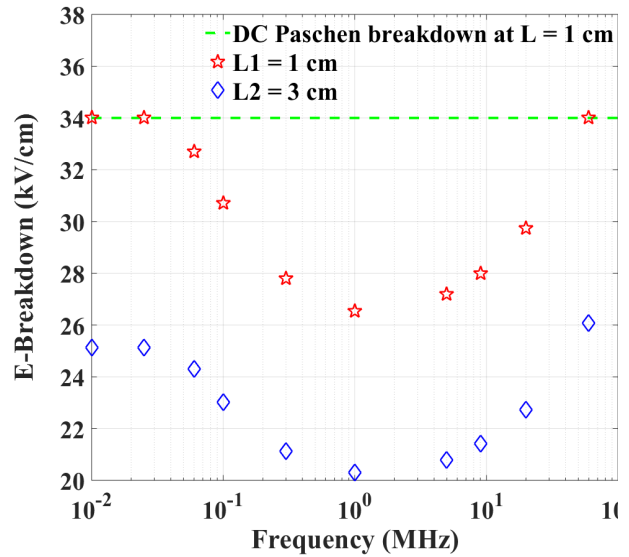


Figure 49. Simulation results obtained for the breakdown field strength versus operating frequency for two different gap lengths. The low frequency value of ~ 34 kV/cm for a 1 centimeter gap approaches the reported DC Paschen limit.

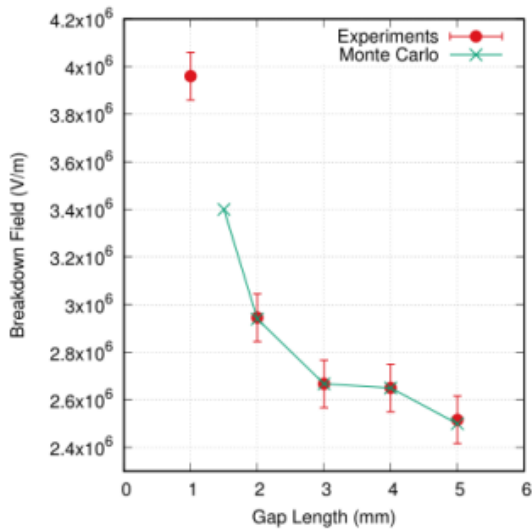


Figure 50. Simulated breakdown field vs gap length compared to measured results at 3.3 MHz.

4C. Studies of MW-class Vacuum Gridless Electron Tubes (Tetrodes, Pentodes and Inductive Output Tubes)

4C (a) Propagation of annular electron beams through the pipes with decelerating gaps

The theory describing the propagation of annular electron beams through the pipes with decelerating gaps is developed. This theory includes both the analytical approach and numerical simulations performed by using the 2D code Michelle.

A typical geometry of the device, which we call a gridless tetrode (in our case it is also known as an inductive output tube), is shown in Fig. 51(a), where the key elements of the device (electrodes and propagating electron beam) are shown. The colors on the beam indicate the beam energy. Fig. 51(b) shows the phase space illustrating the axial momentum of electrons in an annular beam as the function of the axial coordinate.

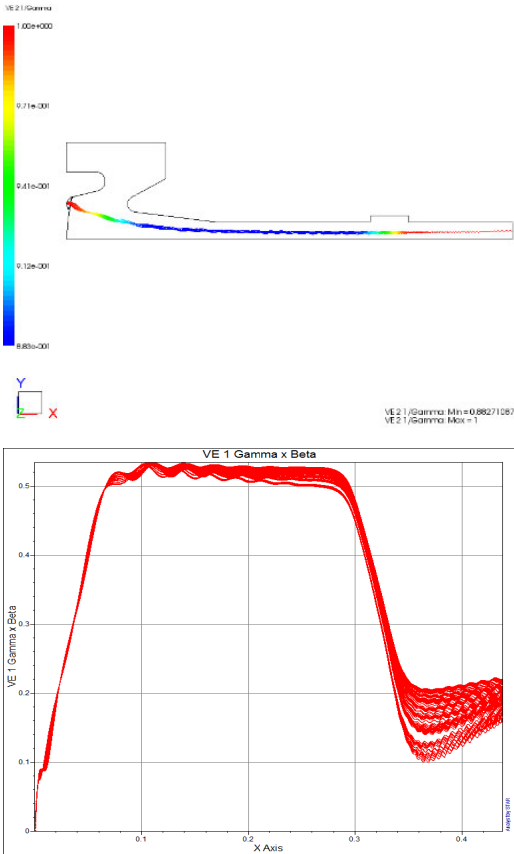


Figure 51. (a) Propagation of an annular electron beam in the device with a nonuniform magnetic field (Model B described below); (b) axial momentum of electrons as a function of the axial coordinate.

As seen in Fig. 51(b), first, electrons acquire the kinetic energy in the region between the cathode and anode, which is shown in Fig. 51(a). Then they propagate with the constant axial momentum in the drift space, after which they enter the region of the decelerating gap where they lose significant portion of the axial energy. Finally, they regain some energy in the collector region, when they approach the metallic wall of the collector. We studied the dependence of the interaction efficiency on the beam thickness and its clearance from the inner wall of the pipe and on the width of the decelerating gap.

4C (b) Interaction efficiency of the device

The interaction efficiency of the device was analyzed in three models: Model A – the device with the uniform focusing external magnetic field in the region from the emitter to the collector, Model B – the device with a nonuniform magnetic field produced by a relatively short solenoid, and Model C – the device without any focusing magnetic fields. The first two models were studied assuming that the focusing magnetic field is in the range of 1.0-1.5 kG. It was found that in the case of the optimal choice of parameters the maximum interaction efficiency (in the absence of secondary electrons) can be as high as 93% in Model A and be about 90% in Model B. This maximum value of the efficiency is restricted by the appearance of the reflected innermost electrons in the case of higher decelerating voltages in the gap. In Model C, where we studied, as in Models A and B, the propagation of a 70 kV, 30 A beam it was found that such beam cannot propagate through the interaction space, part of it is reflected due to the space charge forces lowering the beam potential. So only propagation of a 15 A is possible. This situation can be resolved by adding an additional modulating anode, which transform our tetrode into a pentode. The configuration of such a gridless pentode is shown in Fig. 52.

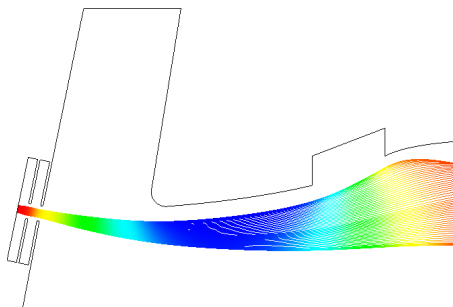


Figure 52. Possible configuration of a gridless pentode with the walls of the anode and the decelerating gap followed by the collector (not shown) shaped in accordance with the geometry of the annular electron beam expanding due to the space charge forces in the absence of focusing magnetic fields.

The shape of electrodes shown in Fig. 52 is profiled in accordance with the shape of a 70 kV, 30 A propagating in the absence of focusing fields. The maximum interaction efficiency of such a device is close to 91%. All simulations reported above correspond to the case when there is no secondary electrons.

4C (c) Role of secondary electrons in the device operation

The role of secondary electrons produced in the collector region was studied by using the time dependent version of the PIC code Michelle. We considered the device operating in class D mode (in each RF period the current pulse duration is less than $\frac{1}{4}$ of this period, see Fig. 53A). It was found that when the beam current is on (Fig. 53B), secondary electrons emitted from the collector are driven back into the collector by the incoming primary beam. However, when the primary beam is switched off (Fig. 53C), secondary electrons can stream into the interaction space that slightly lowers the efficiency. Nevertheless, since in the region between the cathode and the anode there is the DC field accelerating electrons in the positive z-directions, the secondary electrons do not reach the emitter. A proper shaping of the anode also allows one to avoid interception of the secondary electrons by the anode, as shown in Fig. 53C.

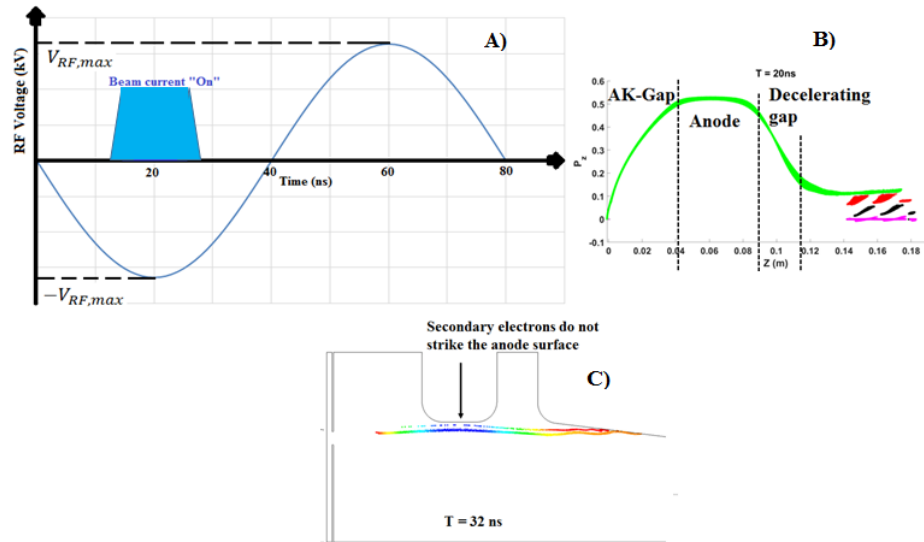
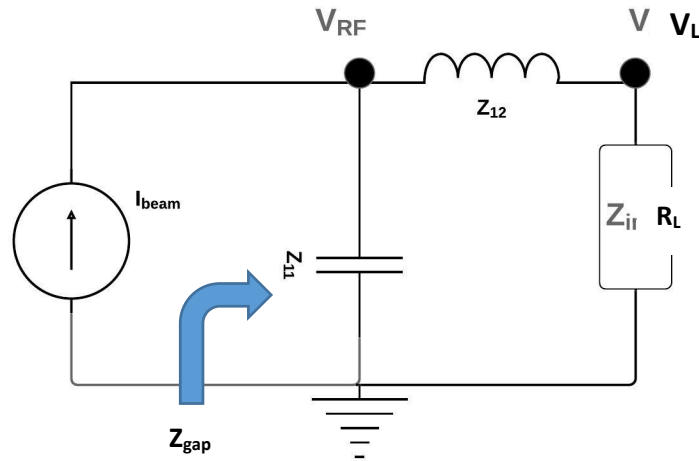


Figure 53. (a) The RF voltage and beam current dynamics during one full cycle; (b) Axial momenta of primary (green) and three generations of secondary (red, black and pink) electrons at 20 ns; (c) propagation of secondary electrons in the absence of primary electrons at 32 ns (the anode is properly shaped).

4C (d) Extraction circuits

The resonant extracting circuit in an RF tube extracts kinetic energy of the modulated electron beam and converts it into electromagnetic energy. For the application considered here, mobile low frequency sources (3 - 10 MHz) for ionospheric heating, high efficiency is important, and thus class D operation is desired. The broad frequency range requires the circuit to be tunable, and the need for a constant decelerating voltage requires constant impedance. In 2016, we discussed our work on how transformers coupled with capacitors acted as a resonant circuit. The report also discussed how the inter-winding capacitances of the transformer created a low reactance path from the secondary to the primary and consequently contributed to the significant power dissipation in the primary windings. This acted as deterrent to the high efficiency we intend to obtain. In 2017 we discussed the design and construction of a pi-circuit that combines the best features of transformer based resonant circuit and provides control over the undesirable stray capacitances. While the pi-circuit provided resonance with low stray capacitances, it posed stringent restrictions on the winding resistance of the coil for a low loss system. Also, the bandwidth of operation was narrow and prone to detuning. This report discusses the design of a more elegant power extraction circuit based on first principles. It provides us control over all aspects of the circuit design: impedance, resonant frequency, quality factor, tunability and bandwidth and is less restrictive on winding resistance.

In Fig. 54, the concept of a single stage power extraction design is shown that can achieve tunability, constant impedance and high efficiency used for power extraction from the IOT is shown.



4.

Figure 54. Circuit diagram of the single stage L circuit used for the power extraction from the IOT

The L circuit is a typical way to enhance the impedance from the load side to the source side. By adding a pair of inductors and capacitors as shown in the figure, we can either enhance or reduce the impedance as seen from the source side. Hence, the resonant frequency and gap impedance are both controlled by the two lossless elements. Hence, we have to vary both the elements to tune the system to a different frequency. To achieve low loss, coil resistance should be low compared to the load. Though the quality factors of the coils used in the L circuit is relatively

lower compared to pi circuit (almost 4 times lower at 3 MHz frequency), we can further reduce the restriction by using multistage L circuits (shown in Figure 55).

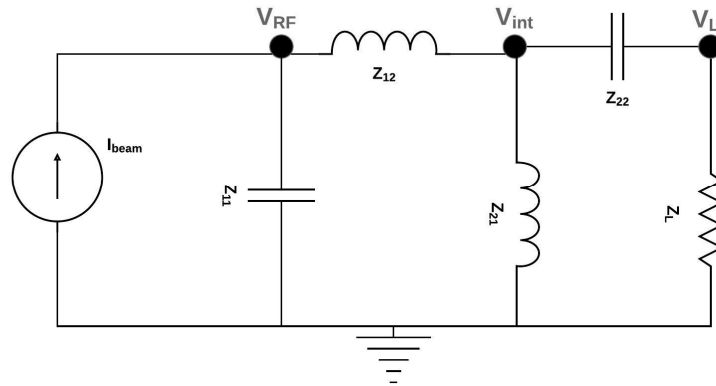


Figure 55. Circuit diagram of the two-stage L circuit

The multistage L circuits give us good control over the tunability, gap impedance and quality factor of the coils in comparison to pi circuits (almost 10 times lower at 3 MHz).

4C (e) Experimental studies

Experimental measurements were performed on a pi-circuit extraction resonator connected to an electron gun (shown in Fig. 56) on loan from Naval Research Laboratory (NRL). This experiment is a scaled-down, proof-of-principle testing of the pi-circuit to be used as a tunable power extraction device for the bunched electron beam. The NRL gun is a gridded thermionic cathode that was originally designed to operate with a cathode-anode voltage from 10 to 35 kV with a cathode-grid voltage 10 – 200 V. We were able to drive the grid directly through its biasing electrode (about -30 V relative to the cathode) with square pulses of small duty factor (25 %), peak voltage of 80 V, at the 3 – 10 MHz RF frequency range.

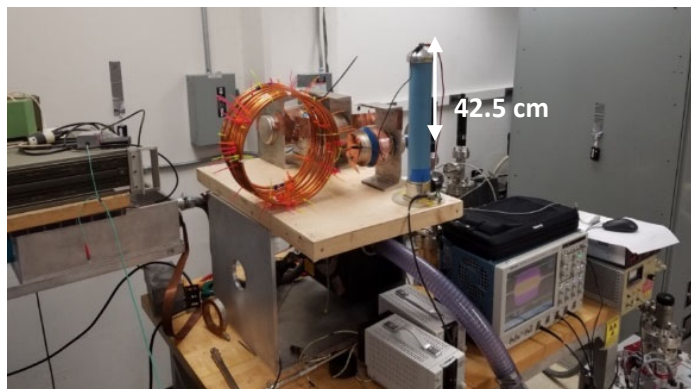


Figure 56. Pi-Circuit extraction resonator and low power electron gun.

The electron beam in our experiment propagated through a 24 cm drift section embedded in a short (10 cm) solenoidal magnetic field providing 300 Gauss at 8 A. The diverging beam is mildly focused by the solenoid and then the beam hits a collector plate isolated from ground using a high voltage feed through. The pi-circuit was composed of an inductor, L_{12} made from copper

tubing and a vacuum variable capacitor (VVC) for C_1 , and two VVC's in parallel for C_2 . The output load was 50Ω and the input RF voltage induced in the pi-circuit on C_1 is measured with a 1000:1 voltage divider into the oscilloscope. The measured RF voltage V_{RF} induced on the input capacitor C_1 of the pi-circuit is shown in Fig. 57(a) for a C_2 of 1.0 nF (near maximum output power).

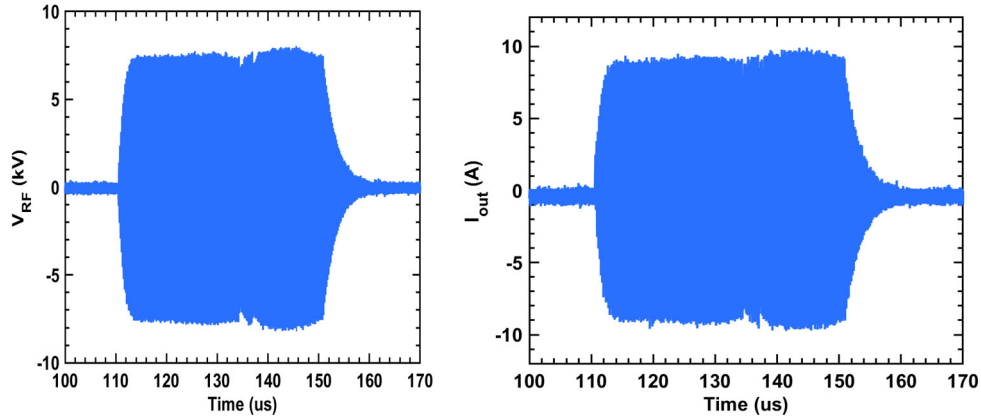


Figure 57. Measured V_{RF} (a) and I_{out} (b) versus time from the pi-circuit.

The V_{RF} waveform has an envelope that increases over several microseconds and decays similarly when the drive RF pulses have ended. The rise and fall times of the envelope are related to the Q-factor of the pi-circuit where the power loss is from both the power in the output resistor and the internal resistance of the inductor. Similarly, the measured output current I_{out} is shown in Fig. 57(b). By varying the capacitance of C_2 , we were varying the input impedance and as a result the induced V_{RF} . Figure 58(a) shows the input and output powers and Fig. 58(b) shows the efficiency inferred at various capacitances for C_2 , at an RF drive frequency of 5 MHz.

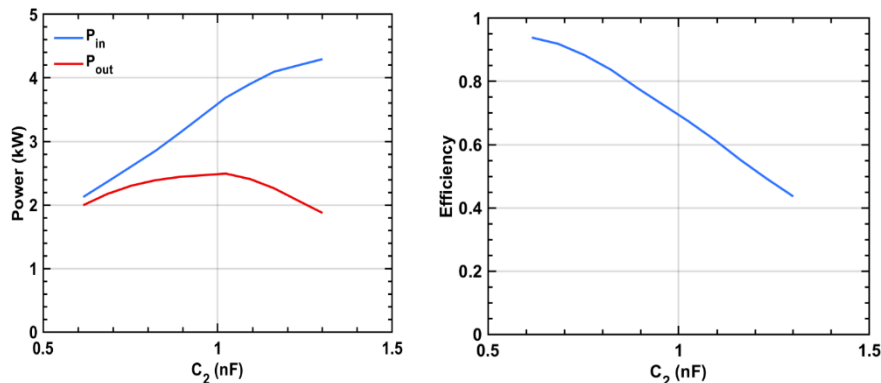


Figure 58. Input and output power (a) and efficiency (b) versus capacitance C_2 at an RF drive frequency of 5 MHz.

When the capacitance of C_2 was decreased, the voltage induced V_{RF} also decreased but the transfer efficiency of the circuit increased to 96.5%. At higher transfer efficiencies, there was less power stored in the resonator and correspondingly less power being lost in the resistive component of the inductor (low Q). When the pi-circuit is tuned to maximize output power, the efficiency drops to 70% and as a result, more power is dissipated in the inductor (higher Q). Figure 59 illustrates the measured Q at various capacitances for C_2 , at an RF drive frequency of 5 MHz.

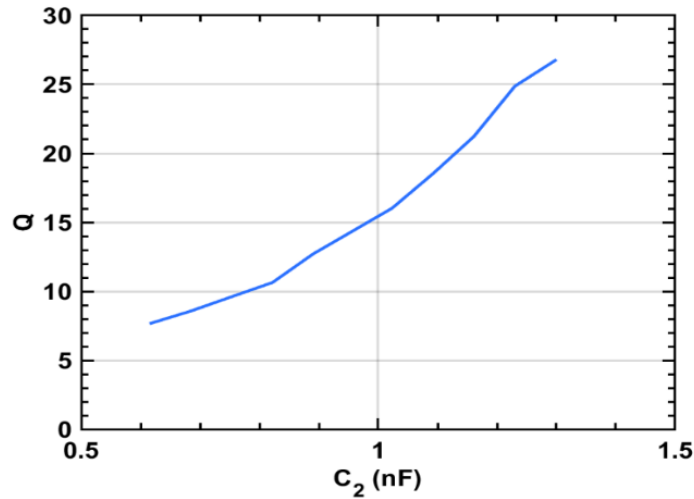


Figure 59. Measured Q versus capacitance C_2 at an RF drive frequency of 5 MHz. The measured Q of the circuit spans a range from 7 to 27. By sweeping C_2 we vary the induced V_{RF} and consequentially extract more kinetic energy from the beam at larger C_2 's.

Concluding note to the experiments with the NRL gun. In terms of a MW class RF source required for IM research, the required gap impedance Z_{gap} will be significantly lower as compared to the gap impedance needed for the low power experiments presented here using the NRL electron gun. Calculations and cold test measurements have shown the pi-circuit needed for the 70 kV, 30A device is significantly less sensitive to the parasitic losses in the inductor as the beam impedance is substantially smaller.

4C (f) Artist's rendition of a MW-class device

Artist's rendition of Model C device, a compact device that does not require a solenoid for beam focusing or the additional power supply, is shown in Fig. 60.

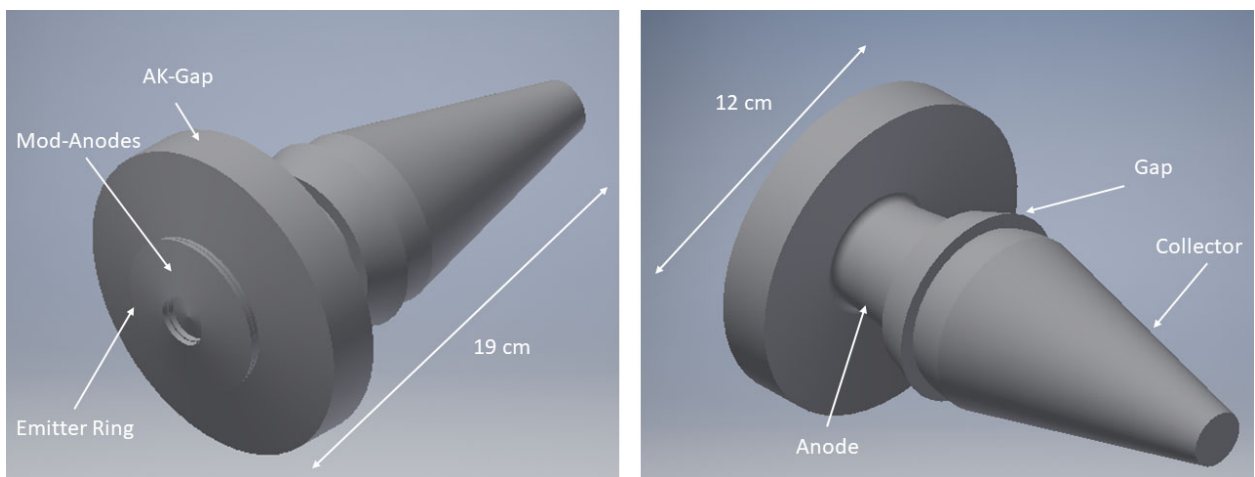


Fig. 60. Artist's rendition of Model C device.

5. MAJOR DEVELOPMENTS AND FINDINGS

- Development of and laboratory testing of a new and novel antenna for injection of EMIC waves from space-based platforms, including the ISS and CubeSats. Laboratory tests in the LAPD chamber demonstrated the new antenna, named Ferrite Loop Antenna (FLA), exceeds the performance of conventional loop antennas by more than 30dB. It is expected that under inner RB conditions it can trigger nonlinearly EMIC waves with amplitude exceeding 10 nT. Such waves can play a major role in remediating the inner RB following an accidental or deliberate High Altitude Detonation (HAND) or Carrington solar storm. (The paper describing the laboratory proof-of-principle of the FLA was selected as *Scilight* by the editor of the Review of Scientific Instruments)
- Design of EMIC space based injection antenna based on *Single Domain Magnetic Nanoparticles (SDMN)* and referred here as *Magnetic Nano-Transmitter (MNT)*. *SDMN* are small (10-20 nm radius), single domain, noninteracting magnetic grains with uniaxial magnetic anisotropy, dispersed in medium viscosity or solid non-conducting matrix. They can be described as ensembles of noninteracting magnetic moments that when driven by an AC magnetic field, behave in a manner similar to ordinary paramagnets, with the exception that *SDMNs* are composed by many thousands of magnetic atoms and as a result have susceptibilities comparable to ferromagnets but with very low coercivity and almost no hysteresis loss. Depending on the size and matrix viscosity they can have response time smaller than msec. Theoretical analysis shows that an assembly of 50-50 Co-Fe *SMDN* diluted to 15% in epoxy and driven by 1.5A AC current will perform with an order of magnitude higher efficiency and a factor 10 smaller weight than the FLA. The relative high cost of the *SMDN* prevented laboratory testing of the *MNT* concept.
- Discovery of a novel Virtual Antenna concept based on controlled Cerenkov emission operating in equatorial regions without the need for electrojet.
- Major advances in generating Artificial Ionospheric Turbulence (AIT). This includes generation and detection of super-small striations (~10 cm) by F-region HF heating at high latitudes using the HARP heater as well as Upper Hybrid predictions for equatorial regions. Such striations can cause serious scintillation effects on GPS transionospheric links.
- Design specifications for Transportable Heater arrays for important DoD applications as a function of geomagnetic latitude.
- Theoretical analysis and numerical modeling with the use of the time-dependent code Michelle resulted in formulating the concept of a compact, gridless pentode capable of operating without focusing magnetic fields. Such a device driven by a 70 kV, 30A electron beam can operate in the class D mode at 0.5 MW power level with the efficiency about 90% at frequencies from 3 to 10 MHz.

- It was shown that for realizing high (more than 90%) efficiency in all frequency range the circuit for extracting the RF power from the vacuum electron RF device should be configured as a multi-stage L-circuit.
- Experimental measurements were performed on a pi-circuit extraction resonator connected to an electron gun on loan from Naval Research Laboratory (NRL). This experiment is a scaled-down, proof-of-principle testing of the pi-circuit to be used as a tunable power extraction device for the bunched electron beam. The solid-state driver for this experiment was designed and fabricated by the student Charles Turner (UMd). It was shown that such a circuit can operate with efficiencies exceeding 90%. In the devices driven by 70 kV, 30A electron beams such circuits will operate even better because the circuits will be less sensitive to parasitic losses in the inductors.

6. *COLLABORATORS, STUDENTS, PAPERS*

The list of collaborators, students, papers published in refereed journals (38) and invited and contributed presentations is given in Addendum